

Analytical Predictive Model for the Long-term Bond Performance of CFRP Tendons in Concrete

Citation:

Toumpanaki, E., Lees, J.M. And Terrasi, G.P. (2020). Analytical Predictive Model for the Long-term Bond Performance of CFRP Tendons in Concrete *Composite Structures*. 2020, *to appear*

Version:

Accepted for publication

Please cite the published version when available.

Analytical Predictive Model for the Long-term Bond Performance of CFRP Tendons in Concrete

Eleni Toumpanaki¹, Janet M. Lees², Giovanni P. Terrasi³

Abstract

The bond between Carbon Fiber Reinforced Polymer (CFRP) tendons and concrete depends on the resin mechanical properties that can degrade under environmental conditions. An analytical model to predict the combined effects of temperature and humidity fluctuations on the bond behaviour of CFRP tendons embedded in concrete is presented. The interaction between a CFRP tendon and concrete is studied by considering different competing mechanisms such as tendon swelling and plasticisation effects due to the concrete internal humidity, differential thermal expansion, concrete autogeneous shrinkage, Poisson's ratio effects and radial bond stresses generated during the pulling out of a tendon from concrete. The analytical bond failure predictions correlate reasonably well with experimentally observed radial-cracking failure modes of CFRP tendons in high strength concrete. Matrix plasticisation appears to influence the long-term bond strength of FRP rods in normal or high strength concrete. Swelling and shrinkage effects become significant in uncoated tendons due to their impact on the frictional bond component. Deviations between measured and predicted bond strength values are attributed to a possible overestimate of the moisture-induced swelling expansion of CFRP tendons. The research findings suggest the introduction of environmental bond factors to consider durability effects in the design of FRP prestressed concrete structures.

Keywords: CFRP, analytical model, durability, bond strength

¹ Lecturer in Civil Engineering, Department of Civil Engineering, University of Bristol, Queen's Building, University Walk, Bristol, UK, BS8 1TR, Tel:+44(0)1173315202, e-mail: eleni.toumpanaki@bristol.ac.uk (corresponding author)

² Professor, Department of Engineering, University of Cambridge, Trumpington Street, Cambridge, UK, CB2 1PZ, e-mail: jmL2@eng.cam.ac.uk

³ Professor, Laboratory for Mechanical Systems Engineering, Swiss Federal Laboratories for Materials Science and Technology (EMPA) and visiting Professor at the University of Edinburgh, School of Engineering, UK Überlandstrasse 129, 8600 Dübendorf, Switzerland, e-mail: giovanni.terrasi@empa.ch

1 Introduction

The U.S Federal Highway Administration (FHWA) concluded that steel corrosion is prevalent in every U.S. industry sector including infrastructure and transportation. The associated repair and maintenance costs were estimated to be billions of dollars per year [1]. The impact of related social factors including traffic disruption give rise to even greater economic ramifications.

The use of Carbon Fiber Reinforced Polymer (CFRP) tendons in humid environments presents a good alternative to steel tendons due to the corrosion-free properties of CFRP materials. CFRP prestress tendons have already been used in a range of structural concrete applications including bridges e.g. Beddington Trail Bridge [2] and prestressed lighting poles [3]. Design guidelines have been proposed in the USA [4], in Canada [5], in Japan [6] and by the International Federation for Structural Concrete [7,8].

Prestressed concrete applications are advantageous since the tensile strength and strain capacity of the CFRP materials are more fully exploited [9] and the deflections of the structural members can remain within the serviceability criteria. In pretensioned applications, the prestress force is transferred to the concrete through the bond between the CFRP tendons and concrete. The bond performance of CFRP tendons depends on their matrix component where most failure modes lie. FRPs are susceptible to moisture uptake due to the porous structure of the matrix and this leads to potential swelling expansion and a decrease in the matrix mechanical properties.

The alkalinity, internal humidity, permeability and cracking of surrounding concrete will influence the tendon moisture absorption [10, 11, 12]. The FRP and concrete contact behaviours are inter-dependent and hence the outcomes for FRP tendons embedded in high strength concrete (HSC) will differ from normal strength concrete (NSC) due to inherent differences primarily in permeability, shrinkage and tensile strength.

Current studies on the bond durability of CFRP tendons have investigated environmental effects either separately (e.g. thermal loads in [13]) or used FE models [14]. The current analytical study investigates the combined effects of exposure to humidity and temperature fluctuations on the bond strength and failure modes of CFRP tendons embedded in concrete. Normal and high strength concrete are considered to provide indicators such as the role of the concrete in the resistance to internal cracking, shrinkage and moisture availability around a tendon. FRP expansion/contraction from environmental and loading effects, matrix degradation due to exposure in concrete internal humidity and a sand coverage component (mechanical interlocking effect) are also reflected. The analytical findings are compared with experimental results of pull-out test samples with either FRP rods or tendons exposed to water.

2 Radial dimensional influences due to environmental and loading effects

The bond pull-out behaviour of CFRP tendons in high strength concrete specimens exposed to temperature or moisture is influenced by competing radial dimensional effects at the FRP/concrete interface. In the following, thermal, moisture-induced swelling, concrete shrinkage, and tensile loading transverse effects are discussed.

The maximum uniform temperature of a concrete bridge deck can be up to 50°C [15], whereas the surface concrete temperature of a CFRP prestressed concrete pole exposed to sun has been measured to be as high as 60°C [16]. The longitudinal coefficient of thermal expansion of carbon-epoxy composites is controlled by the fibers and is regularly cited as being negative [17] or zero. So it is generally considered to be negligible. However, the transverse coefficient of thermal expansion (CTE) of CFRP tendons can be up to 3-6 times greater than that of concrete [18]. Concrete cracking and spalling due to a 30°C rise in temperature has been reported [13] in GFRP reinforced concrete due to the thermal expansion of a GFRP rebar ($D=13$ mm) with a high transverse coefficient of thermal expansion (CTE) of $58 \mu\epsilon/^\circ\text{C}$. For temperature rises above the glass transition T_g of the epoxy in CFRP bars, plasticisation of the matrix and bond strength degradation take place [19].

Bare CFRP tendons have been found to swell in diameter when subjected to water [20] but the moisture availability at the bond interfaces is affected by the concrete permeability or cracking. The effects of swelling expansion of FRP bars exposed in a concrete humid environment on the bond strength and bond failure modes are difficult to isolate. Sen et al. [14] suggested that localised swelling due to moisture absorption at cracks resulted in bond failures of CFRP pretensioned beams tested in flexure (4-point loading) after 9 months of exposure of pre-cracked beams at 63-75% of their ultimate capacity in simulated tidal conditions. However, bond failures were not observed at longer exposure times and this was attributed to non-Fickian diffusion mechanisms from microcracking of the epoxy matrix and fiber-matrix debonding. The presence of epoxy cracking created paths of moisture subsidence within the CFRP. GFRP bars have been found to exhibit a smaller bond strength degradation at 60°C as compared with a similar exposure regime at 23°C when pull out test specimens were exposed in tap water. This was attributed to a greater moisture absorption at higher temperature such that the swelling improved the mechanical interlocking and frictional bond component [21].

A beneficial effect of concrete shrinkage on the bond performance in high strength concrete has been reported in

studies on steel or FRP bars (22, 23). However, the shrinkage restraining effect in FRP bars is lower than with steel due to the lower transverse elastic Young's modulus [24]. Sayed et al. [23] argued that the shrinkage effect is not as pronounced in CFRP bars tested in bond after 3 and 90 days in ultra high performance fibre reinforced concrete (f_c at 3days=120 MPa). This was believed to be due to high early age concrete autogenous shrinkage taking place mostly after 0-3 days.

CFRP tendons are susceptible to a strain change in the transverse direction when loaded in tension (Poisson's ratio effect) due to their anisotropic behaviour and lower longitudinal elastic Young's modulus. During pulling out of a CFRP tendon in tension, there can be a non-uniform stress distribution through the cross-section due to the lower shear stiffness of the external resin rich surface layer compared with the fiber-matrix shear stiffness of the core tendon. This results in higher strain values at the interface between concrete and CFRP tendons and higher axial stresses and interfacial bond stresses (Figure 1a) [25].

Bond forces between the CFRP tendon and concrete develop at an angle α from the tendon axis as shown in Figure 1b. The radial component of the bond forces (splitting forces) can be considered as a pressure acting on a thick-walled concrete ring. Tepfers [26] proposed three bond scenarios. In the elastic uncracked phase (Figure 1c) the tangential stresses are calculated based on an elastic thick walled cylinder analysis. In the partly-cracked elastic phase (Figure 1d) radial cracks have developed but do not extend to the concrete surface. In the plastic stage (Figure 1e) a bond failure occurs when the concrete tensile strength has been reached throughout the concrete ring. The latter scenario is more likely with low concrete strengths and small concrete covers [26].

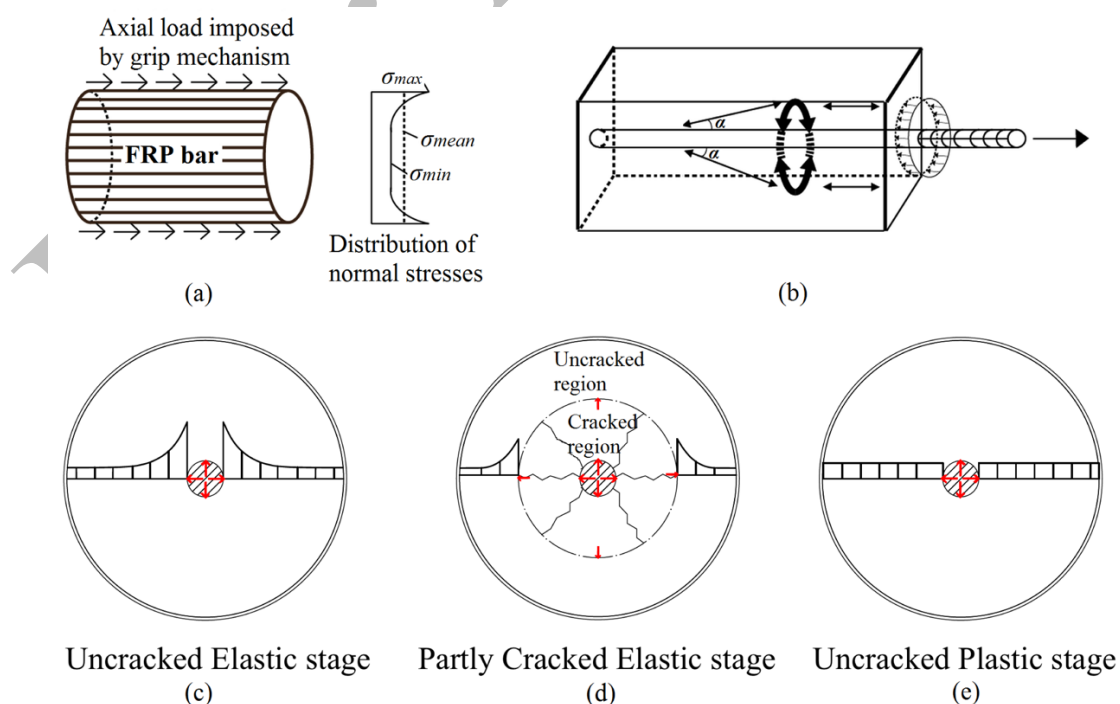


Figure 1:(a) Non uniform axial stress distribution in an FRP bar in tension (after [25]), (b) Bond radial stress component (after [54]) and tensile stress distribution in (c) elastic uncracked stage, (d) partly cracked elastic stage (e) plastic stage (after [54]).

2.1 Thick-walled cylinder analysis

In this study a thick-walled cylinder approach is adopted to model the environmental and loading conditions at the FRP/concrete interface. Swelling and thermal effects and concrete autogeneous shrinkage are superposed to model an unloaded immersion phase and ascertain whether radial cracking occurs. A pull-out testing phase where additional Poisson's ratio effects and bond radial stresses then follows as shown schematically in Figure 2a.

Peer reviewed

the two materials is defined as p_k . The solid CFRP tendon has an outer radius r_o and is surrounded by a concrete annulus with internal radius r_o and external radius r_l . To calculate the pressure p_k associated with each of the phenomena of interest, it is necessary to satisfy radial deformation compatibility between the CFRP tendon and concrete. In the elastic uncracked stage (EU) of a thick walled analysis, the radial deformation of a CFRP tendon subjected to an external pressure p_k is given by:

$$\Delta r_t = \frac{r_o p_k}{E_{T_FRP}} (1 - \nu_{T_FRP}) \quad (1)$$

where Δr_t is the radial change of the tendon, E_{T_FRP} is the transverse Young's modulus of the CFRP tendon and ν_{T_FRP} is the transverse Poisson's ratio of the CFRP tendon.

Following the same thick walled analysis, the change in radius of a concrete annulus, Δr_c , can be derived:

$$\Delta r_c = \frac{r_o p_k}{E_c} \left(\frac{r_l^2 + r_o^2}{r_l^2 - r_o^2} + \nu_c \right) \quad (2)$$

where E_c is the Young's modulus of the concrete and ν_c is the Poisson's ratio of the concrete.

In the partly-cracked elastic stage (PC) the formation of cracks up to a critical radius $r_{cr}=0.48r_l$ [28] leads to the following equation for the change in radius of the cracked concrete ring at the vicinity of the tendon ($r_o < r \leq r_{cr}$).

$$\Delta r_{c,cr} = \frac{r_o p_k}{E_{c,cr}} \ln\left(\frac{r_{cr}}{r_o}\right) \quad (3)$$

where $E_{c,cr} \approx E_c/2$ is the assumed Young's modulus of the cracked concrete. Equation 3 is valid until $p_k=0.30f_{ct}r_l/r_o$ where full cracking of the concrete cover takes place [28]. Due to the exceedance of the tensile concrete strength the hoop stresses are assumed to be zero in the cracked region.

2.2 Deformation compatibility and matrix softening

The pressure, p_k , due to the restricted expansion or contraction at the tendon/concrete interface associated with each of the radial deformation influences needs to be calculated. This pressure is derived from the deformation compatibility equations from an unrestricted free radial deformation, Δr_k , as shown in Figure 3. A 'k' subscript is used to denote each influence where $k=swell$ for swelling effects from the moisture uptake in the CFRP tendon, $k=sh$ for the concrete autogenous/drying shrinkage, $k=\Delta T$ for temperature effects, $k=poisson$ reflects the transverse Poisson's ratio effects during pulling out and $k=bond$ indicates the bond bearing stresses. A negative tendon pressure (e.g. due to thermal expansion) leads to positive tensile concrete hoop stresses, $\sigma\theta_c$. The

physical phenomenon and relevant analytical expressions adopted here are discussed in the following. A particular contribution in the current work is that moisture effects are explicitly taken into account through consideration of the availability of moisture due to the concrete internal humidity, the initial moisture content in the tendon, any ingress of moisture from external exposed concrete faces, and the subsequent diffusion through the tendon. This understanding allows for moisture-induced swelling of the tendon and matrix softening effects to be quantified.

		Self-stress		Free deformation	Deformation compatibility	Scheme	
		stresses	CFRP				Concrete
Unloaded conditions	Swelling	$-p_{swell}$ $\sigma_{\theta_c} (+)$			$\Delta r_{swell}(t) = \epsilon_{swell}(t)r_o$	$\Delta r_i + \Delta r_c = \Delta r_{swell}(t)$	
	Autogenous shrinkage	$-p_{sh}$ $\sigma_{\theta_c} (+)$			$\Delta r_{sh}(t) = \epsilon_{sh}(t)r_o$	$\Delta r_i + \Delta r_c = \Delta r_{sh}(t)$	
	Temperature	$-p_{\Delta T}$ $\sigma_{\theta_c} (+)$			$\Delta r_{\Delta T}(t) = \epsilon_{\Delta T}(t)r_o$	$\Delta r_i + \Delta r_c = \Delta r_{\Delta T}(t)$	
Loaded conditions	Poisson's effect	$p_{poisson}$ $\sigma_{\theta_c} (-)$			$\Delta r_{poisson} = \epsilon_{poisson} r_o$	$\Delta r_i + \Delta r_c = \Delta r_{poisson}$	
	Radial bond component	$-p_{bond}$ $\sigma_{\theta_c} (+)$			N/A	$\Delta r_i + \Delta r_c = \Delta r_{bond}$	

Figure 3: Radial deformations and compatibility conditions

2.2.1 Concrete Internal Humidity

After casting, the concrete internal humidity changes. In high strength concrete, a decrease in the internal humidity (H) in the central concrete core surrounding an embedded CFRP tendon takes place as hydration proceeds with time and moisture movement becomes limited due to the inherent low permeability. In normal strength concrete, the water surplus due to the high water/cement ratios (usually for $w/c > 0.38$ where capillary pores start to develop [29]) results in high internal relative humidity levels above 95%. For immersed concrete specimens with CFRP reinforcement water ingress through the concrete can take place leading to radial moisture diffusion through the tendon.

The concrete internal humidity has been modelled and experimentally verified by Zhang et al. [30] for normal (C30) and high strength (C80) concrete based on Fick's laws. Assuming a constant concrete diffusion

coefficient, D_c , independent of the pore humidity, the following equation is derived for one-dimensional diffusion in the x - axis.

$$\frac{H - H_s}{H_d - H_s} = \text{erf}\left(\frac{x}{2\sqrt{D_c t}}\right) \quad (4)$$

where x is the coordinate with respect to the external exposed concrete face, H is the concrete internal humidity,

$$H_s = \begin{cases} 1 & \text{for } \alpha \leq \alpha_c \\ (H_{s,u} - 1) \left(\frac{\alpha - \alpha_c}{\alpha_u - \alpha_c}\right)^\beta + 1 & \text{for } \alpha > \alpha_c \end{cases}$$

is the concrete humidity from self-desiccation due to hydration, $H_{s,u}$ is

the concrete humidity from self-desiccation at the ultimate degree of hydration, $\alpha_u = \frac{1.031w/c}{0.194 + w/c}$ is the ultimate

degree of hydration as a function of water/cement ratio (w/c), $\alpha = \alpha_u \exp\left[-\left(\frac{A}{t}\right)^B\right]$ is the degree of cement

hydration, α_c is the critical hydration at curing time t_c , when the concrete humidity starts to decrease from 100%,

A , B and β are empirical constants and H_d is the environmental humidity. Under wet curing conditions or full

immersion in water $H_d = 1.0$ and when air curing or exposure to ambient conditions takes place $H_d = RH/100$.

The diffusion coefficient D_c can be calculated using the concrete sorptivity, S . When an external concrete face is

exposed to water and a constant diffusivity is assumed, the relationship between the sorptivity S and D_c is

derived [31] as:

$$S/\sqrt{D_c} = 2/\sqrt{\pi} = 1.128 \quad (5)$$

Sorptivity values are typically determined experimentally using methods such as ASTM C1585 [32] where one

face of a preconditioned concrete specimen is exposed to water and the mass uptake with time is measured.

Equation 4 can be solved numerically by subdividing the concrete section in segments of width $h=1$ mm and the

humidity of each node $H_i(t)$ at each time step Δt is calculated as:

$$H_i(t+\Delta t) = H_i(t) + \frac{D_c \Delta t}{h^2} (H_{i-1}(t) - 2H_i(t) + H_{i+1}(t)) + (H_s(t) - H_s(t+\Delta t)) \quad (6)$$

The humidity of the first concrete surface node, $i=1$, exposed to the environment as proposed by Zhang et al.

[30] is

$$H_1(t) = \frac{hH_d + (D_c/\alpha_m)H_2(t-1)}{h + D_c/\alpha_m} \quad (7)$$

where α_m is a surface factor that influences the transportation of water on the surface layer.

In our model the humidity of the last node n at the FRP/concrete interface will affect the moisture content within the CFRP and thus the bond mechanism through swelling.

2.2.2 Time-dependent radial diffusion through CFRP tendon

Prior to casting, a bare CFRP tendon will have an internal moisture profile that is a function of the storage environment and history. In the current work the initial concentration $C(r)$ from the ambient storage conditions will be taken to be a constant, C_I , through the tendon cross section. Hence $C(r)=C_I$ at $0 \leq r < r_o$ and $t=0$. An initial moisture content can be represented as an offset:

$$C_I = \frac{M_{init}}{M_{sat}} \quad (8)$$

where M_{init} is the initial moisture content and M_{sat} is the mass at the saturation point of a previously desiccated CFRP tendon.

After casting in concrete and immersion in water, the moisture concentration at the CFRP/concrete boundary and thus radially through the tendon is expected to vary with time due to any wetting or drying. Any longitudinal diffusion into the CFRP tendons through an exposed end immersed in water (e.g. in a pull out test specimen immersed in water) is expected to be limited due to the high fibre volume content [33] and will therefore not be considered further in the analysis.

A time-varying input $C(r)=H_{rc}(t)$ at $r=r_o$ and $t \geq 0$ is adopted, where H_{rc} is the humidity profile of the concrete node n at the reinforcement/concrete interface that depends on the moisture availability in the concrete. A schematic representation is shown in Figure 6a.

Crank [31] has proposed a closed form expression to calculate the time-dependent concentration profile through a cylindrical rod subjected to a varying surface concentration, $C(r_o)=H_{rc}(t)$. However, the resulting analytical solution is complex. Instead an incremental numerical method based on Crank's expressions [31] for a rod with a constant external concentration is adopted in the current work. Two concurrent boundary conditions are applied. Full saturation conditions at the tendon surface corresponding to concrete casting are initially imposed. There is then a step-by-step decrease in the surface humidity concentration with curing time. The steps can be summarised as:

- 1) Calculate the moisture concentration gradient in the tendon by assuming full saturation at the boundary $C(r_o, t)=C_{co}=1$ for a given time t_o .
- 2) Calculate the surface moisture concentration $C(r_o, t_o)=H_{rc}(t_o)$ at the outer radius $r=r_o$ due to the drop in internal concrete humidity over curing time t_o .
- 3) Calculate an average time-step decrease in surface concentration after curing time t_o ,

$$dC(r_o, t_o)=(C_{co} - C(r_o, t_o))/t_o \text{ at } r=r_o$$

4) The concentration gradient along the CFRP radius within the tendon is then given as:

$$C(r,t_o)=C_I+(C_{co}-C_I)\left\{1-\frac{2}{r_o}\sum_{n=1}^{\infty}\frac{1}{\alpha_n} \frac{J_o(r\alpha_n)}{J_1(r_o\alpha_n)}e^{-D_{22}\alpha_n^2 t_o}\right\} - \sum_{t=1}^{t=t_o}\left(\frac{C_{co}-C(r_o,t_o)}{t_o}\right)\left\{1-\frac{2}{r_o}\sum_{n=1}^{\infty}\frac{1}{\alpha_n} \frac{J_o(r\alpha_n)}{J_1(r_o\alpha_n)}e^{-D_{22}\alpha_n^2 t}\right\} \quad (9)$$

where t_o is the concrete curing/exposure time of the CFRP tendon in a concrete humid environment, D_{22} is the tendon diffusion coefficient, α_n are the roots of the Bessel function $J_o(r_o\alpha_n)=0$, r_o is the radius of the CFRP tendon, C_I the initial constant moisture concentration in the tendon. A gradual change with exposure time takes place. For example, assuming a time step of 1 day, a step decrease in the surface concentration $dC(r_o,t_o)$ will act over an exposure period $[0,1]$ day, the second will act over $[0,2]$ days until the final step decrease from $[0,t_o]$ days where an equilibrium surface concentration $C(r_o,t_o)$ is reached. Using this superposition method there is moisture movement between the tendon surface and the centre of the CFRP tendon as the tendon surface concentration changes with exposure time. The time dependent concentration at the outer radius of the CFRP tendon ($r=r_o$) is assumed to act uniformly over the perimeter and length of the CFRP tendon. The mass uptake M_{t_o} at a given time t_o , is derived by integrating the concentration gradient $C(r,t_o)$ over the circular cross-section.

2.2.3 Tendon swelling

Once the mass uptake is known, a relationship between the swelling expansion strain in CFRP tendons and the moisture uptake can be applied. Based on experimental data derived for bare CFRP tendons immersed in deionised water at 20°C, Scott and Lees [20] proposed that:

$$\varepsilon_{t,swell}(\%)=0.363M_t(\%) + 0.0073 \quad (10)$$

Although the relationship was developed from full immersion conditions in water, as a simplification, it will be assumed to also apply irrespective of the different nature of the concrete humid environment.

2.2.4 Matrix softening

In addition to swelling effects, moisture absorption in CFRP tendons can cause matrix plasticisation and degradation. To account for the matrix softening in the transverse Young's modulus (matrix dominated property) the following relationship was adopted as a function of the moisture concentration within the CFRP tendon.

$$E_{T,i}(t) = E_{sat} + (1 - C_{avi}(t))(E_{To} - E_{sat}) \quad (11)$$

where $E_{T,i}(t)$ is the transverse Young's modulus after exposure time t in a discretised ring i in the rod's section, E_{sat} is the transverse Young's modulus at the saturation point, E_{To} is the dry transverse Young's modulus and C_{avi} is average moisture concentration of a discretised ring i in the rod's cross section. Equation 11 is based on an analytical model for the torsional shear modulus degradation (matrix dominated property) in CFRP tendons after full immersion in water in [10]. The equivalent average transverse Young's modulus of the tendon is calculated based on a strain compatibility approach between adjacent discretised rings of $E_{T,i}$. The change in radius of the last discretised ring at the perimeter of the rod, as derived from the self-stress state of the discretised section, is equal to the relevant radius' change of a tendon with an average plasticised transverse Young's modulus E_{Teq} . Therefore, concrete tensile stresses generated by the swelling of an FRP rod are reduced due to the plasticisation phenomena in E_T leading to a more accurate prediction of concrete cracking and interfacial pressure p_k .

2.2.5 Concrete shrinkage

In a low permeability high strength concrete, autogenous shrinkage is expected to occur due to withdrawal of water from the capillary pores during hydration even when concrete is exposed in water. In normal strength concrete, autogenous shrinkage is more limited due to the higher pore network structure and greater number of available paths for moisture from the external environment to penetrate in. The autogenous shrinkage $\varepsilon_{csh}(t)$ as a function of time can be calculated using the Eurocode 2 [34] expression:

$$\varepsilon_{csh}(t) = \beta_{ash}(t) \varepsilon_{csh,inf} \quad (12)$$

where $\varepsilon_{csh,inf}$ is a function of the concrete characteristic cylinder strength at 28 days $2.5(f_{ck,cyl} - 10)10^{-6}$ and $\beta_{ash}(t)$ is a coefficient that depends on the age of the concrete t where $\beta_{ash}(t) = 1 - \exp(-0.2t^{0.5})$. The equation for drying shrinkage $\varepsilon_{cd}(t)$ based on Eurocode 2 [34] is:

$$\varepsilon_{cd}(t) = \beta_{ds}(t, t_s) k_h \varepsilon_{cd,0} \quad (13)$$

where $k_h = 1.0$ is a coefficient that depends on the notional size $h_o = 2A_o/u$ in mm,

$\beta_{ds}(t, t_s) = (t - t_s) / ((t - t_s) + 0.04 \sqrt{h_o^3})$, where t age of concrete at the time considered in days and t_s is the age of

concrete at the beginning of drying shrinkage. Note that Eurocode 2 [34] suggests that the final unrestrained drying shrinkage or swelling expansion is negligible at $RH=100\%$ for normal strength concrete (CEM class N) irrespective of the value of concrete strength.

2.2.6 Temperature

The thermal unrestricted strain at the tendon/concrete interface due to an elevation of temperature can be calculated as:

$$\varepsilon_{AT} = (\alpha_t - \alpha_c) \Delta T \quad (14)$$

where α_t and α_c are the coefficient of thermal expansions of the tendon and concrete respectively and ΔT is a rise in temperature in °C.

2.2.7 Poisson's ratio effect

Assuming pure axial loading on a tendon, the change in radial strain due to the Poisson's ratio effect is:

$$\varepsilon_{poisson} = \nu_{T_FRP} \frac{\sigma_L}{E_{L_FRP}} \quad (15)$$

where ν_{T_FRP} is the Poisson's ratio of the CFRP tendon, σ_L is the axial tension and E_{L_FRP} is the longitudinal Young's modulus of the CFRP tendon. When an external sand coating layer is present, tensile stresses at the interface between the sand coating layer and the core tendon may develop due to chemical adhesion between sand particles and concrete.

2.2.8 Radial bond component and bond strength degradation

During the pull out of a CFRP tendon from the concrete, bearing stresses develop in the concrete at an angle α with respect to the FRP tendon axis (Figure 4). These bearing stresses (Figure 4b & 4d) are decomposed into a longitudinal component $p' \cos \alpha$ that represents the bond shear stresses and $p' \sin \alpha$ is a radial component that represents the splitting bond stresses (Figure 4c) and $p_{bond} = \tau \tan \alpha = p_k$. The angle α depends on the surface profile of the FRP tendon. Experimental results for sand coated GFRP bars have shown that an angle of $\alpha = 30^\circ$ can be adopted [26]. In the case of smooth tendons, no bearing stresses are expected to develop and therefore $\alpha = 0$. Although the axial bond component might vary due to relative slip between the tendon and the concrete, in the current work the bond stress is assumed to be constant along the bonded length.

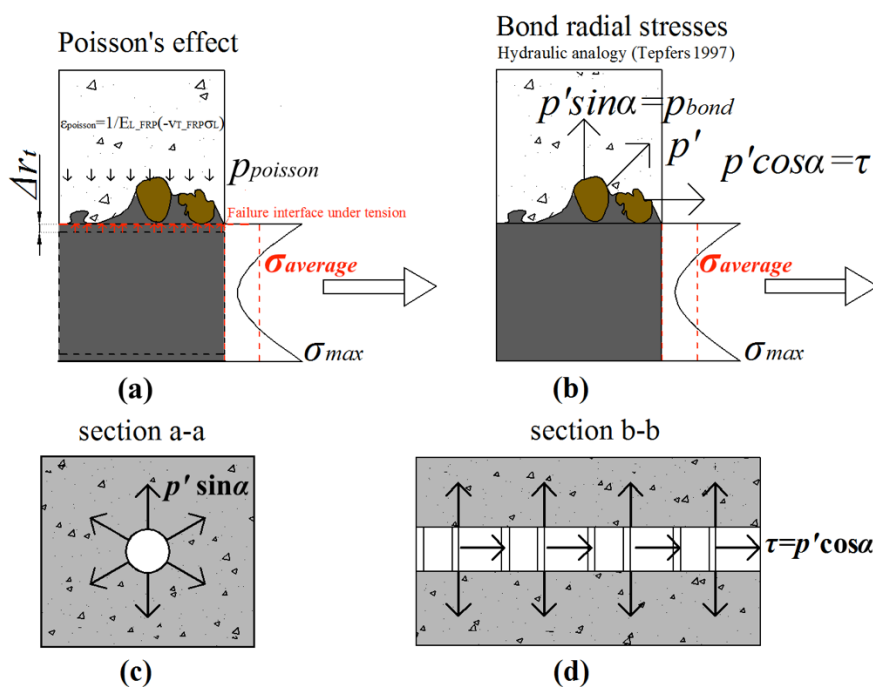


Figure 4: (a) Poisson's ratio effects, (b) Bearing stresses in a sand coated CFRP tendon, (c) Radial splitting stresses-section a-a and (d) Radial and shear bond stresses-section b-b.

The bond strength loss due to matrix softening due to moisture exposure is modelled by adapting a torsional shear modulus degradation model proposed in [10].

$$\tau_{pl}(t) = \tau_{sat} + \frac{\sum_{i=1}^n (1 - C_{avi}) I_i}{I} (\tau_o - \tau_{sat}) \quad (16)$$

where $\tau_{pl}(t)$ is the bond strength after exposure time t , τ_{sat} is the bond strength at the saturation point, τ_o is the reference bond strength (theoretical dry value) and I_i is the second moment of area of a discretized ring in the rod section and I is the second moment of area of the rod. In Equation 16 the second moment of area is adopted in lieu of the polar second moment of area originally considered in [10]. The former is considered as more representative of the shear lag effect in the bond performance of FRP rods (non-uniform axial stress distribution).

3 Analytical bond durability model

3.1 Validation of bond failure modes

Most existing studies on the assessment of FRP bond strength after exposure in environmental conditions report the overall average bond failure mechanism. However, it is difficult to isolate whether any internal cracking at the tendon concrete interface occurred due to moisture exposure and/or bond pull-out. An exception was

Toumpanaki et al.'s [35] microscopic observations of radial cracking over time of CFRP tendons embedded in high strength concrete and exposed to wet environments at 23°C or 40°C. Three types of CFRP tendons with different diffusion and thermal expansion properties were studied allowing for these parameters to be investigated. The influence of wet or dry curing, exposure time and temperature can also be probed as both conditions were represented in the experimental work. The associated experimental concrete and tendon properties and processing and exposure conditions [35] were therefore used as input parameters in the analytical model to validate the failure modes. However, since only high strength concrete was used in [35], predictions are also made for FRP rods embedded in normal strength concrete using further studies available in the literature. This enabled a comparison of the effect of different concrete grades (HSC vs NSC) on the bond durability performance of FRP specimens.

3.1.1 Input parameters

3.1.1.1 FRP specimen properties

The material and mechanical properties of the CFRP tendons are summarized in Table 1. The initial tendon moisture content was fixed as $M_{init}=0.5\%$ as derived from the drying of lab conditioned samples from groups C-UN and D. These values lead to a constant initial concentration gradient of $C_I=0.24$ and 0.37 for the C-UN and C-SL and D tendons respectively. However it should be noted that the assumptions for the M_{sat} values might deviate due to the presence of an external resin rich sand coating layer in the sand coated tendons but the same epoxy material as in the core tendon is used.

Table 1. Tendon properties

Parameter	CFRP		
	C-UN	C-SL	D
Initial condition	Uncoated	Originally sand coated	Originally sand coated
Matrix/Epoxy Hardener	Bakelite EPR 4434/EPH 943	Bakelite Rutapox 4539/	Bakelite EPR 4434/EPH 943
Fibres	Tenax UTS 5631	Tenax UTS 5131	Tenax UTS 5631
Nominal core tendon diameter (mm)	4.2	4.2	5.4
Quartz sand coating-Grain size (mm)	-	0.4-0.63	0.4-0.63
Volume fraction	0.64	0.63	0.64
Ultimate tensile strength-average (MPa)	1913 ⁽¹⁾	2733 ⁽¹⁾	1913 ⁽¹⁾
Longitudinal Elastic modulus – E_L (GPa)	No data	163	155.7
Transverse Young's modulus – E_T (GPa)	6.16 ¹	6.16 ¹	6.16 ¹

Poisson's ratio – ν_T	0.27 ⁽²⁾	0.27 ⁽²⁾	0.27 ⁽²⁾
Coefficient of thermal expansion (CTE) – α_T ($\mu\epsilon/^\circ\text{C}$)	26.5 ⁽²⁾	32.5 ⁽¹⁾	26.5 ⁽²⁾
Diffusion coefficient – D_{22} (cm^2/sec)	1.92×10^{-10} ⁽³⁾	1.46×10^{-10}	1.46×10^{-10} ⁽³⁾
Mass uptake at saturation – M_{sat} (%)	2.10 ⁽³⁾	1.36	1.36 ⁽³⁾

Note 1: ⁽¹⁾ from [36], ⁽²⁾ from [37] ⁽³⁾ from [33]

Note 2: Differences in the ultimate tensile strength between C-SL and D and C-UN groups might be attributed to the tensile testing (e.g. gripping effects) and not necessarily to the epoxy and fibre component.

3.1.1.2 Concrete mechanical properties

Wet cured and air cured high performance concrete batches with a low w/c ratio (w/c=0.3) were used in [35].

The mix proportions of the batches were the same but there was some variation in the amount of plasticiser and the extent of vibration during casting. The measured concrete cube strengths varied from $f_{cm,cube} = 55.9 \pm 2.6$ MPa after immersion in a water tank at 23°C for 7 days to $f_{cm,cube} = 75.4 \pm 1.1$ MPa after 14 days of air curing by sealing with plastic sheeting at $19.7 \pm 1.1^\circ\text{C}$ and $RH = 52 \pm 6.7\%$.

In absence of experimental data, the strength of the C25/30 NSC was selected to be 25 MPa regardless of the curing conditions. The associated mean tensile concrete strengths were analytically calculated based on Eurocode 2 [34]. The supporting references used to calculate the concrete Young's modulus, Poisson's ratio and coefficient of thermal expansion are summarised in Table 2. The mixes are designated as W, A and A/W for wet, air and air/wet curing conditions accordingly.

3.1.1.3 Pull out test specimens

A concrete ring of $r_f = 50$ mm is based on a pull out test specimen $100 \times 100 \times 100$ mm with a 40 mm bonded length [35]. The internal tendon radius, r_o , varied according to the type of CFRP tendon. After casting, the CFRP/concrete specimens were exposed over time in water for up to 72 weeks at either 23°C or 40°C. Control specimens were tested after either wet curing for 7 days (groups C-UN and C-SL) or air curing at $19.7 \pm 1.1^\circ\text{C}$ and $RH = 52 \pm 6.7\%$ (group D) for 14 days.

3.1.1.4 Concrete shrinkage

Drying shrinkage effects were neglected for fully immersed HSC concrete samples. Drying shrinkage was, however, calculated in HSC-A/W concrete where samples had been initially air cured for 14 days (69 μm). The age at the onset of drying shrinkage t_s was taken as 1 day. The nominal unrestrained concrete drying shrinkage, $\epsilon_{cd,0}$, in HSC-A/W was derived using a linear interpolation from Table 3.2 in Eurocode 2 [34] for $RH=52\%$ and

C90/105. The same principles and *RH* assumptions were used to calculate $\varepsilon_{cd,0}$ in NSC-A. Any accelerated concrete ageing mechanisms in HSC for samples exposed in water at 40°C were not considered. In the calculation of the shrinkage strain the actual exposure time at 40°C, t , and the respective concrete strength ($f_{ck,cyl}=0.85f_{cm,cube}-1.64STDV$ where STDV is the standard deviation) are taken into account in Equation 12 and 13.

Table 2: Concrete Properties

Parameter	NSC		HSC	
	W	A	W	A/W
$f_{ck,cyl}$ (MPa)	25.00 ^{3,4}	25.00 ^{3,4}	68.00 ^{3,5}	75.00 ^{3,5}
f_{ctu} (MPa)	2.60 ⁶	2.60 ⁶	4.10 ⁶	4.30 ⁶
E_c (GPa)	31 ⁴	31 ⁴	39 ⁴	39 ⁴
ν_c ⁷	0.185	0.185	0.185	0.185
w/c	0.54	0.54	0.30 ¹	0.31 ¹
Exposure regime	Wet curing	Air curing	Immersion in a water bath at 23/40°C ¹	Air curing by sealing with plastic sheeting at 19.7 ± 1.1°C and RH=52 ± 6.7% (14 days) followed by immersion in water bath at 23/40°C ¹
$\varepsilon_{cd,0}$ (x10 ⁻⁶) ⁶	0	510	0	230
$\varepsilon_{csh,inf}$ (x10 ⁻⁶) ⁶	37.5	37.5	144.5	162.4
$H_{s,u}$ ²	0.95	0.95	0.45	0.45
t_c (days) ²	7.0	7.0	3.0	3.0
α_m (cm/day) ²	3.00	3.00	4.70	4.70
A ²	19.73	19.73	13.00	13.00
B ²	0.68	0.68	0.80	0.80
β^2	1.50	1.50	1.80	1.80
D_{ci} (mm ² /s)	1.26x10 ⁻⁰⁵	1.26x10 ⁻⁰⁵	4.44x10 ⁻⁰⁷	4.44x10 ⁻⁰⁷
D_{cs} (mm ² /s)	3.14x10 ⁻⁰⁶	3.14x10 ⁻⁰⁶	1.26x10 ⁻⁰⁷	1.26x10 ⁻⁰⁷

Note: ¹from [35], ²from [30], ³ values after 28 days of curing, ⁴ from [34], ⁵ $f_{ck,cyl}=0.85f_{cm,cube}-1.64STDV$, ⁶ $f_{ctu}=2.12\ln(1+f_{cm}/10)$ for HSC and $f_{ctu}=0.30f_{ck,cyl}^{2/3}$ for NSC according to EC2 [34], where f_{cm} is the mean compressive cylinder strength = $0.85f_{cm,cube}$ [38] and $f_{ck,cyl}$ is the characteristic compressive cylinder strength, ⁷ from [38].

3.1.1.5 Concrete sorptivity

Water absorption tests according to ASTM C1585 [32] were carried out in HSC-W after 7 days of initial wet

curing. The initial and secondary sorptivity values, the curing age, the curing conditions and the respective concrete strengths are summarised in Table 3. The resulting initial and secondary sorptivities for a concrete batch cured after 7 days at 23 °C are 0.0012 and 0.0004 mm/s^{1/2} respectively. The secondary sorptivity S_s decreases with increasing curing age and temperature. Similar secondary sorptivity values in the range of 0.0003-0.0008 mm/s^{1/2} have been reported elsewhere [39] for concrete with ordinary Portland cement and a low w/c ratio of 0.35, air cured for 28 days and conditioned at 80% RH for 14 months. The concrete diffusion coefficient calculated using Equation 5 and based on the secondary sorptivity after 7 days is $D_c=1.26 \times 10^{-07}$ mm²/sec.

Table 3. Sorptivity values from water absorption tests for HSC-W mix

Specimen	Curing temperature (°C)	Curing age (days)	Primary sorptivity S_i [mm/s ^{1/2}]	Secondary sorptivity S_s [mm/s ^{1/2}]	Concrete strength f_{cu} (MPa)
PE_23_1	23	7	0.0012	0.0004	55.9
PE_23_2	23	28	0.0006	0.0003	87.2
PE_23_3	23	70	0.0009	0.00015	99.2
PE_40_1	40	28	0.00045	0.0003	102.9
PE_40_2	40	70	0.00075	0.00004	98.9

Note: PE_a_b: a denotes the curing temperature of 23 or 40°C and b denotes the specimen identification.

In normal strength concrete the sorptivity values are typically much higher than in HSC. Initial and secondary sorptivity values of 0.004 and 0.002 mm/s^{1/2} respectively have been reported in [39] in normal concrete with w/c=0.4-0.5 after conditioning at RH=65% and 23°C for 14 months. This corresponds to initial and secondary concrete diffusion rates of $D_c=1.26 \times 10^{-05}$ mm²/sec and $D_c=3.14 \times 10^{-06}$ mm²/sec respectively and these values are adopted here for NSC.

3.1.1.6 Concrete Internal Humidity

Based on equation 6, the concrete humidity in the vicinity of the CFRP bonded region was predicted as a function of time for both normal and high strength concrete. All the empirical constants and assumptions of the model are summarised in Table 2. Any initial differences in the curing regime (e.g. air/wet curing) were also accounted for the environmental humidity, H_a . The humidity profiles with respect to the x-coordinate from the exposed concrete face ($x=0$) to the rod/concrete interface ($x=50-r_o$) are depicted in Figure 5a for both NSC and HSC and for the specified curing regimes after 14 and 548 days (1.5 years). It can be seen that the curing regime (wet vs air curing) has a negligible effect on the concrete internal humidity distribution in HSC. The differences in the concrete internal humidity gradient are more pronounced in NSC with increasing curing time. Even after

1.5 years of full immersion in water the concrete internal humidity at the CFRP/concrete interface is greater than 0.91 and 0.45 for NSC and HSC respectively irrespective of the curing regime. Figure 5b shows the humidity distributions, H_{rc} , with increasing curing time at the vicinity of the CFRP bonded region ($x=47.3$ mm) for all concrete mixes.

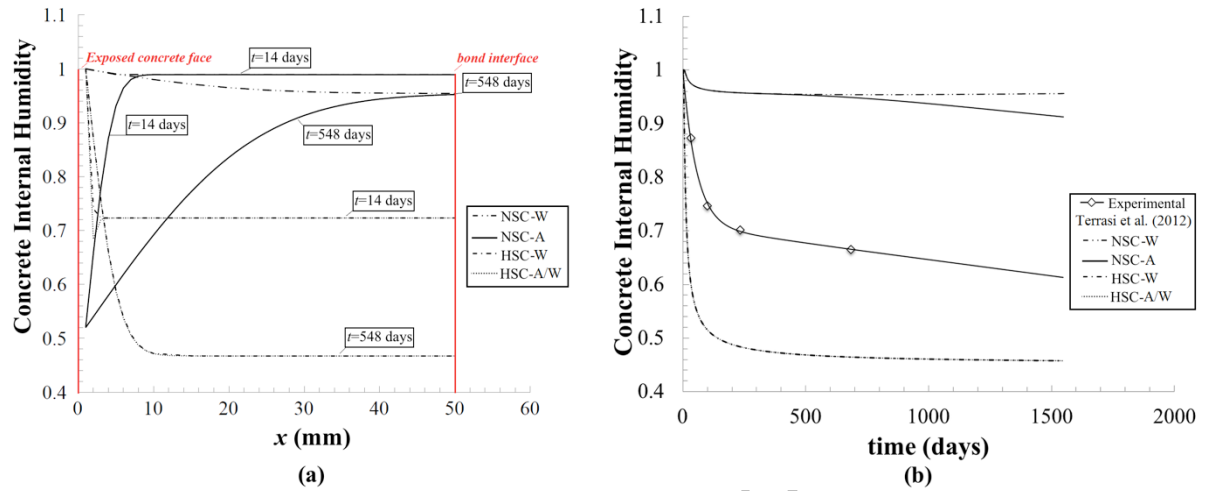


Figure 5: Concrete internal humidity (a) along the x -axis (b) at the concrete/FRP rod interface ($x=50$ mm) with respect to curing time.

Experimental concrete internal humidity measurements are also included in Figure 5b from 500 mm long samples in concrete slabs cast with a self-consolidating concrete mix, similar to the HSC one that is used in the experimental part of this study, and air cured at ambient conditions [40]. A best fit exponential curve based on the Least Squares method applied to the experimental data presented in [40] yielded with $R^2=0.99$:

$$H_{rc}=0.29e^{-0.01804t}+0.71e^{-0.00009515t} \quad (17)$$

Equation 17 with humidity values greater than 0.67 up to 684 days is adopted in the analytical bond failure model for HSC and Equation 18 applies for NSC. The latter was derived by adopting the same type of exponential curve as above and following the same method.

$$H_{rc}=0.04e^{-0.02182t}+0.96e^{-0.0000024t} \quad (18)$$

3.1.1.7 Time-dependent radial diffusion through CFRP tendon

The predicted concentration gradients and mass uptakes due to the internal humidity of the concrete are shown in Figure 6. Since there were two different exposure temperatures, 23°C and 40°C, time shift factors were used to convert 40°C tendon moisture uptake results into equivalent exposure times at 23°C. The applied time shift factors (TSF) used are 3.5 and 3.1 for groups C-UN and C-SL and D respectively. More details can be found in [35]. Allowing for an initial moisture concentration offset, the subsequent time-dependent concentration

gradients through the C-SL, D and C-UN tendons at specific equivalent exposure times at 23 °C for HSC are depicted in Figure 6 (b) and (c) respectively. The additional time of curing for all specimens that was used as a reference state for the exposure programme (1 week for HSC-W and 2 weeks for HSC-A/W) has also been considered in the exposure time. For ease of comparison the concentration gradient of the C-UN group in NSC-W is also included in Figure 6(c). The average tendon moisture content as a function of time due to the concrete internal humidity (this is in addition to the initial moisture content) in both HSC and NSC is shown in Figure 6(d). After 221 weeks of equivalent exposure at 23°C in specimens C-SL the concentration gradient decreases towards the outer tendon surface (Figure 6b) and a small increase in the mass uptake (11%) is observed compared with 72 weeks of exposure. This is the result of the decreasing relative humidity in HSC with time. A uniform concentration profile at $C \approx 0.65 \approx H_d$ seems to be reached at longer exposure times (e.g. after 144.6 weeks of equivalent exposure at 23°C for group D). At similar exposure times group C-SL and D exhibit similar concentration gradients along the radius but higher concentrations are reached at the centre of the tendon in the smallest diameter (Figure 6b). The moisture profile of C-UN tendons in NSC-W shows that the outer section of the tendons is more prone to plasticisation (e.g. $C > 0.9$) and bond failures within the matrix can be favoured with increasing exposure time as experimentally observed in [41] for uncoated tendons. The highest moisture uptake over time is observed in group C-UN due to its higher diffusivity for both concrete grades (HSC and NSC). The CFRP tendons exhibit a higher moisture uptake propensity when embedded in NSC irrespective of the curing regime (e.g. C-SL-NSC-W vs C-SL-NSC-A). The concrete internal humidity at the rod/concrete interface is almost the same for wet and air curing conditions after 144.6 weeks of equivalent exposure at 23°C (≈ 1000 days), as observed in Figure 5b. Small deviations in the concrete internal humidity are observed after 500 days of curing (Figure 5b) but these are not critical for the total moisture uptake of the CFRP tendons. Indicatively, group C-UN exhibits 36% higher moisture uptake after 57 weeks of equivalent exposure in water at 23°C (wet curing) in NSC compared with HSC.

The hoop stresses at the CFRP tendon/concrete interface due to concrete shrinkage, tendon swelling and differential thermal expansion were calculated for the unloaded immersion phase using the approaches detailed in the previous section. If the total hoop stress over time exceeded the concrete tensile strength capacity, concrete radial cracking takes place due to environmental conditions and a partly-cracked analysis (PC) is adopted in the loaded stage. If there is no exceedance of the concrete tensile capacity due to environmental

conditions, an elastic uncracked analysis (EU) is considered and the hoop stress from an experimental pull out load is superposed. If the bearing stresses are high, concrete radial cracking can occur during pull-out testing.

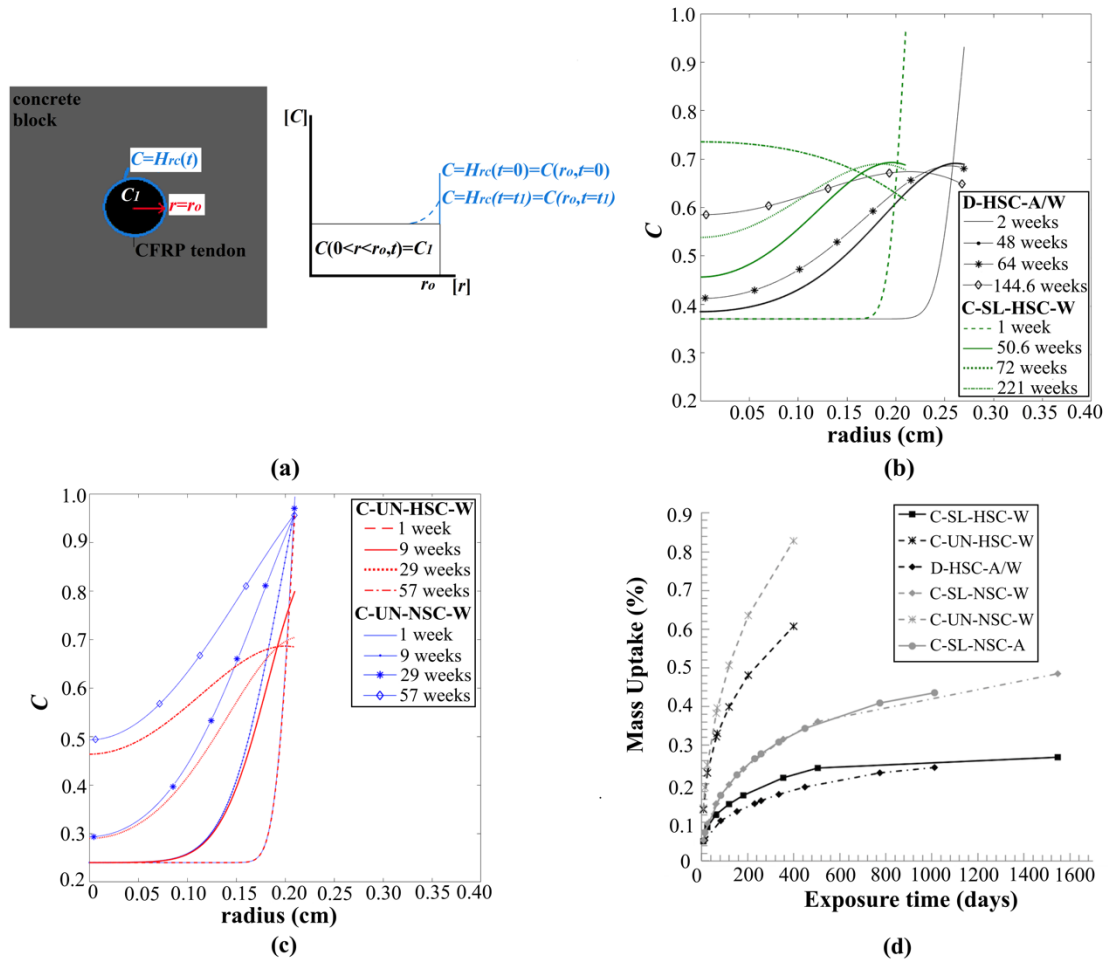


Figure 6: (a) Boundary conditions, concentration gradients due to concrete internal humidity over curing time for (b) C-SL and D in HSC – effect of diameter (c) C-UN in HSC and NSC- effect of concrete grade and (d) Mass uptake over time due to concrete internal humidity.

3.1.1.8 Unloaded conditions

The analytical hoop stresses based on an elastic uncracked thick walled analysis from the time-dependent tendon swelling (adjusted to an equivalent exposure time at 23°C for the 40°C samples), concrete shrinkage and temperature effects are summarised in Table 4. Both HSC and NSC are considered. At roughly similar exposure times, the greatest radial, σ_{r_c} , and hoop, σ_{θ_c} , stresses are observed in group C-UN due to the higher moisture absorption rate in the tendon material. In the C-UN samples the HSC tensile strength is predicted to be exceeded after 9 weeks of equivalent exposure at 23°C. The swelling expansion of the tendons is greater than the shrinkage contraction and is the dominant mechanism leading to higher hoop and radial stresses in concrete that could precipitate a bond radial cracking failure mechanism. The application of elevated temperature (e.g. 40°C) can accelerate concrete radial cracking phenomena in HSC as analytically predicted in groups C-SL and D after 25.8 and 64 weeks of equivalent exposure time at 23°C. Radial cracking is calculated at lower exposure times, if the same tendons are used in NSC (e.g. after 3.5 and 8.7 weeks of equivalent exposure in water at 23°C for groups C-UN and C-SL respectively- see Table 4). This is attributed to the higher swelling expansion of the CFRP tendons in the NSC-W mix combined with the lower shrinkage strains that result in higher hoop stresses exceeding the concrete tensile capacity (almost half of the relevant HSC tensile capacity). However, the air curing conditions (NSC-A) can delay the time to radial cracking (e.g. after 22 weeks of exposure time). This is the result of higher shrinkage strains and lower moisture availability compared with wet conditions (NSC-W) resulting in a stress-relief from the developed interfacial pressure. By comparing C-SL and D with respect to the diameter at similar equivalent exposure times at 23°C (e.g. roughly after 50 weeks) in HSC, C-SL exhibits 30% greater moisture uptake (due to the higher moisture ingress) and thus transverse expansion but group D has a 29% higher diameter. Consequently, the change in radius for both groups is similar. This might not apply at longer exposure times. The observed increase in the radial stresses, $\sigma_{r_c, total}$, under unloaded conditions is an indication of an increase in the bond radial component. This parameter will be used next in the analytical bond failure model and will be discussed further.

25 **Table 4.** Swelling, autogenous concrete shrinkage and temperature effects at different exposure times - Unloaded Conditions.

Time (weeks)	HSC							NSC						
	$\varepsilon_{b,swell}(t) \times 10^{-6}$	$\varepsilon_{csh}(t) \times 10^{-6}$	$\varepsilon_{AT}(t) \times 10^{-6}$	$\sigma\theta_{cs, total}$ (MPa)	$\sigma r_{cs, total}$ (MPa)	Ratio	Analysis	$\varepsilon_{b,swell}(t) \times 10^{-6}$	$\varepsilon_{csh}(t) \times 10^{-6}$	$\varepsilon_{AT}(t) \times 10^{-6}$	$\sigma\theta_{cs, total}$ (MPa)	$\sigma r_{cs, total}$ (MPa)	Ratio	Analysis
	C-UN-W							C-UN -W						
1	555.9	-59.4	N/A	3.03	-3.02	1.0	EU	569.9	-15.4	N/A	3.28	-3.27	1.0	EU
3.5	901.4	-95.3	N/A	4.51	-4.49	1.1	EU	974.2	-23.6	N/A	3.14	-3.13	1.0	PC
9	1240.2	-119.0	N/A	4.40	-4.38	1.5	PC	1459.8	-29.8	N/A	4.66	-4.64	1.4	PC
9.75 ¹	1272.7	-95.3	298	5.78/4.61 ²	-5.76/-4.60 ²	1.9/1.5 ²	PC/PC ²	1510.4	-30.3	298	5.78/4.82 ²	-5.76/-4.80 ²	1.8/1.5 ²	PC/PC ²
17	1519.5	-128.4	N/A	5.41	-5.39	1.8	PC	1909.4	-33.3	N/A	6.04	-6.02	1.8	PC
29 ¹	1819.3	-119.0	298	7.70/6.55 ²	-7.67/-6.53 ²	2.5/2.2 ²	PC/PC ²	2379.1	-35.3	298	8.40/7.45 ²	-8.37/-7.42 ²	2.6/2.3 ²	PC/PC ²
57 ¹	2277.6	-128.1	298	9.29/8.16 ²	-9.26/-8.13 ²	3.1/2.7 ²	PC/PC ²	3080.0	-36.8	298	10.41/9.48 ²	-10.37/-9.45 ²	3.2/2.9 ²	PC/PC ²
	C-SL-W							C-SL-W						
1	259.9	-59.4	N/A	1.21	-1.21	1	EU	266.4	-15.4	N/A	1.45	-1.44	1.0	EU
3.5	389.8	-95.3	N/A	1.76	-1.75	1.5	EU	424.1	-23.6	N/A	2.28	-2.27	0.9	EU
8.7 ¹	506.6	-95.3	400	4.79/2.43 ²	-4.78/-2.42 ²	4.0/2.0 ²	EU/EU ²	606.0	-29.6	400	3.15/1.86 ²	-3.14/-1.85 ²	2.2/1.3 ²	PC/PC ²
9	510.5	-119.0	N/A	2.31	-2.31	1.9	EU	614.1	-29.8	N/A	1.89	-1.88	1.3	PC
17	607.1	-128.4	N/A	2.81	-2.80	2.3	EU	791.8	-33.3	N/A	2.43	-2.42	1.7	PC
25.8 ¹	688.6	-119.0	400	5.64/3.31 ²	-5.62/-3.30 ²	4.7/2.7 ²	PC/EU ²	935.9	-34.9	400	4.13/2.86 ²	-4.11/-2.85 ²	2.9/2.0 ²	PC/PC ²
50.6 ¹	855.2	-128.1	400	6.46/4.17 ²	-6.43/-4.15 ²	5.3/3.4 ²	PC/EU ²	1216.5	-36.6	400	4.94/3.69 ²	-4.92/-3.68 ²	3.4/2.5 ²	PC/PC ²
72	947.9	-142.9	N/A	4.57	-4.56	3.8	EU	1382.1	-37.1	N/A	4.17	-4.15	2.9	PC
221 ¹	1046.2	-142.9	400	4.89/3.39 ²	-4.87/-3.38 ²	4.0/2.8 ²	PC/PC ²	1834.0	-37.5	400	6.63/5.42 ²	-6.61/-5.40 ²	4.6/3.7 ²	PC/PC ²
	D-A/W							C-SL-A						
2	269.2	-85.6	N/A	1.13	-1.12	1	EU	342.0	-264.0	N/A	0.45	-0.44	1.0	EU
12	450.8	-137.8	N/A	1.92	-1.90	1.7	EU	690.1	-467.3	N/A	1.24	-1.23	2.8	EU
22	537.2	-149.3	N/A	2.35	-2.34	2.1	EU	881.4	-501.2	N/A	2.08	-2.07	1.7	EU
33 ¹	613.6	-137.8	298	4.64/2.86 ²	-4.62/-2.84 ²	4.1/2.5 ²	EU/EU ²	1034.6	-516.2	400	3.08/1.74 ²	-3.07/-1.74 ²	2.5/1.4 ²	PC/PC ²
37	638.1	-156.1	N/A	2.88	-2.87	2.6	EU	1081.1	-519.5	N/A	1.88	-1.88	1.5	PC
48	697.8	-158.3	N/A	3.20	-3.18	2.8	EU	1191.8	-525.9	N/A	2.22	-2.21	1.8	PC
64 ¹	768.1	-149.3	298	5.39/3.64 ²	-5.36/-3.62 ²	4.8/3.2 ²	PC/EU ²	1319.5	-531.3	400	3.93/2.61 ²	-3.92/-2.60 ²	3.2/2.1 ²	PC/PC ²
110.5 ¹	899.7	-156.1	298	6.00/4.28 ²	-5.96/-4.26 ²	5.3/3.8 ²	PC/EU ²	1558.4	-538.2	400	4.63/3.32 ²	-4.61/-3.31 ²	3.7/2.7 ²	PC/PC ²
144.6 ¹	952.9	-158.3	298	6.23/4.53 ²	-6.19/-4.51 ²	5.5/4.0 ²	PC/EU ²	1655.3	-540.4	400	4.91/3.61 ²	-4.89/-3.60 ²	4.0/2.9 ²	PC/PC ²

26

27 Note: ¹application of accelerated ageing temperature of 40°C and use of time shift factor of 3.5 and 3.1 for C-UN and C-SL and D groups respectively for the equivalent
 28 exposure time at 23°C, ²without thermal effects, EU: elastic uncracked stage, PC: partly cracked stage of the thick walled analysis

3.1.1.9 Loaded conditions

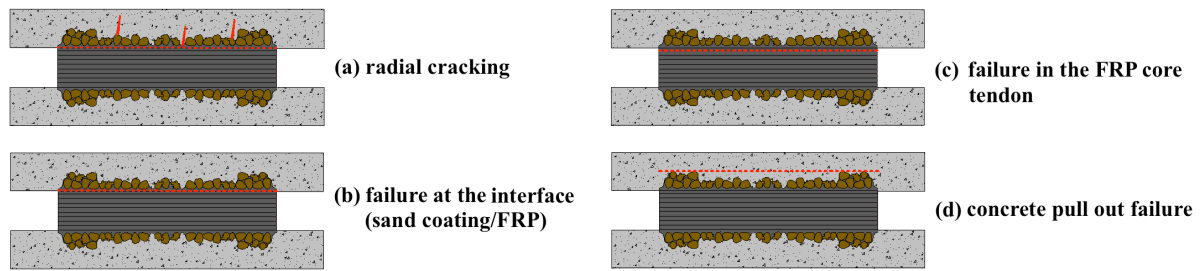
29
 30 The analytical bond durability model was compared against experimental bond durability data for CFRP
 31 tendons presented in [35] for HSC. In Table 5 the strain and stress values due to Poisson's ratio and bond effects
 32 due to a unit applied tensile load of 1 kN are shown. These reference hoop and radial stresses can be multiplied
 33 by the experimental pull out load to derive the actual stress values. For example, for a C-SL specimen where $\sigma\theta_c$
 34 = 0.29 MPa/kN and the load conditions are considered in isolation, an experimental pull out load of
 35 approximately 17 kN would cause cracking at the tendon concrete interface for a concrete tensile strength of ~5
 36 MPa. However, depending on the diameter of the CFRP rod this would be indicative of a 25.1-32.2 MPa bond
 37 strength and higher than experimentally observed values for CFRP sand coated tendons [35] (e.g. 21.0 and 9.9
 38 MPa for group C-SL and D respectively).

39 **Table 5.** Loaded strains

Specimen	$\epsilon_{poisson} \times 10^{-6} / \text{kN}$	p_{bond} (MPa/kN)	$\sigma\theta_c, total$ (MPa/kN)	$\sigma r_c, total$ (MPa/kN)
C-UN	125	0	-0.84	0.84
C-SL	120	-1.09	0.29	-0.29
D	76	-0.85	0.34	-0.34

3.1.2 Discussion

41
 42 In Table 6 the measured maximum bond pull-out failure loads for selected specimens with long exposure times
 43 or a propensity for radial cracking are presented based on [35]. The expected hoop and radial stresses due to the
 44 applied load are also shown in Table 6, as are the total stresses at the pull-out failure load obtained by
 45 superposing the load components and the stresses from Table 5. In Table 6, a temperature effect is not included
 46 for the 40°C specimens since they were cooled down to the ambient laboratory environment of 23°C before
 47 pull-out testing.
 48 The bond failure modes were studied in detail either by splitting open the pull out test specimens or by cutting
 49 samples from the bond failure interface and casting them in fluorescein epoxy under vacuum for inspection
 50 using a Leica DMLM optical microscope. In the latter method, any radial cracking in the concrete layer at the
 51 bonded region could be observed. Four failure modes namely concrete radial cracking (a), failure at the sand
 52 coating/tendon interface (b), failure in the tendon (c) and a concrete pull-out failure (d) were observed. These
 53 failure modes can be schematically seen in in Figure 7. The most common bond failure mechanism for the C-SL
 54 and D sand coated tendons was the shearing off of the sand coating layer (failure mode (b)).



56

57

58

59

60

61

62

63

64

65

66

67

68

69

70

71

72

73

74

75

76

77

78

79

80

81

Figure 7: Possible bond failure mechanisms of exposed CFRP sand coated tendons embedded in concrete (a) radial cracking failure, (b) failure at the sand coating/FRP interface, (c) failure in the FRP core tendon and (d) concrete pull-out failure.

Radial cracking before and after loading is predicted for the uncoated specimens C-UN-HSC-W-40-8, C-UN-HSC-W-23-16 and C-UN-HSC-W-40-16 and radial cracking indicative of failure mode (a) was verified in the specimens in these groups selected for microscopic investigation. The only exceptions lie in specimens C-UN-HSC-W-23-8 suggesting that swelling effects or the diffusivity of the group is overestimated. If the main bond strength mechanism in the uncoated tendons is the friction between the concrete and CFRP tendon, then the bond strength should be linearly correlated with the radial stress σ_{rc} . The C-UN-HSC-W-23-16 group specimens show 28% higher total radial stresses than the C-UN-HSC-W-23-8 specimens using partly cracked elastic thick walled analysis. A respective 18% average increase was recorded in the experimental pull out loads between the two exposure time periods [35]. However, a proportionally linear correlation does not apply, if the C-UN specimens are compared with the control values. Despite the increasing moisture uptake and consequent plasticising effects of the outer epoxy layer with time, bond failure modes within the epoxy matrix were not experimentally observed in the C-UN group. However, it should be noted that the moisture concentration of the outer layers drops down to ~ 0.67 , as depicted in Figure 6c.

The experimental radial cracking failure modes of the sand coated tendons group C-SL and D also correlated reasonably well with the analytical findings. For group C-SL and D specimens, radial cracking would not be expected based on the analytical hoop stresses generated due to the experimental pull out load alone (except for specimen D-HSC-A/W-40-46 (1); pull out load > 17 kN) and nor would it be expected solely due to exposure and shrinkage. Yet, the addition of a temperature rise can cause radial cracking. However, a microscopic examination of an untested group D pull-out test specimen after 46 weeks of exposure at 40°C [35] gave no indication of cracking at the concrete-CFRP tendon interface. So in the C-SL and D specimens exposed at 23°C where a microscopic failure inspection confirmed cracking (C-SL-HSC-W-23-16(2), C-SL-HSC-W-23-71(2),

82 D-HSC-A/W-23-10(2)) it appears that it is the contribution of the developed tensile hoop stresses due to the
83 time-dependent phenomena and the applied load that leads to radial cracking. In a few specimens (e.g D-HSC-
84 A/W-40-10), disagreement of the analytical bond failure model is observed but the analytical hoop stresses, σ_{θ_c} ,
85 were close to the concrete tensile strength within experimental standard deviation.

86 These observations should be considered as indicative trends rather than conclusive results since there is
87 inherent variability, simplifications and further competing factors that could influence the results. The standard
88 deviation in the compressive cube strengths, the possible development of a weaker concrete layer at the sand
89 coating layer interface from air entrapment and the difficulty in inspecting radial cracking by splitting open the
90 specimens should be noted. Another issue in the current work is that the assumed diffusion parameters, mass
91 uptake and dimensional changes were derived from experiments using direct immersion of CFRP tendons in
92 water. But this environment is not representative of the actual humid concrete environment that will be time-
93 dependent. Studies have shown the maximum moisture content in composite materials depends on the RH level
94 of the exposure environment. For example, an increase in RH by 2.7 times at 30°C has been found to yield a
95 tenfold increase in the diffusion coefficient of CFRP laminates with an epoxy Narmco 5208 matrix [42]. It has
96 also been reported that although M_{sat} increases with RH it doesn't depend on the temperature [43, 44]. Swelling
97 expansion in CFRPs seems to be related with the environmental RH . Cairns and Adams [45] reported much
98 lower dimensional changes than Scott and Lees [20] for CFRP composite systems exposed at $RH=98\%$ and
99 $T=65.5^\circ\text{C}$ and the relationship between the swelling expansion strain ($\times 10^{-3}$) and moisture uptake (%) was
100 linearly related with a coefficient $\alpha_I=3.65\times 10^{-3}$. Compressive stresses have been found to reduce the rate of
101 moisture uptake in FRPs so the restrained expansion of a tendon in concrete could affect the mass uptake and
102 hence the expected swelling [46]. Therefore, longer exposure times might be needed to detect concrete radial
103 cracking due to swelling effects alone [41]. However, it should be noted that radial cracking does not always
104 directly correspond with bond degradation since a main bond failure mode in CFRP rods can develop at the
105 sand coating layer interface. A linear elastic fracture mechanics approach with in plane shear crack propagation
106 (mode II) in the resin rich sand coating layer and a crack opening mode I at the concrete FRP interface could be
107 more representative for modelling the crack initiation to full crack development of the resin layer.

108 The accuracy of the thick walled analysis seems to depend on the cover/bar diameter ratio. Chernin and Val [47]
109 contended that thick-walled analytical solutions overestimate the required internal pressure to reach concrete
110 cover cracking and the observed deviation from the FE results increased with increasing cover to diameter
111 ratios. This was attributed to the lack of precision in modelling the non-linear concrete behaviour and the

112 **Table 6.** Analytical bond failure model -Total radial and hoop stresses developed for selected specimens.

Specimen	expos. time (weeks)	equiv. time at	exper. pull out	failure mode	loaded conditions		total		f_{ctt} (MPa)
					σ_{θ_c} (MPa)	σ_{r_c} (MPa)	σ_{θ_c} (MPa)	σ_{r_c} (MPa)	
C-UN-HSC-W-c-0 (1)	control	1	1.94	(b)	-1.64	1.63	1.39 ^{EU}	-1.39 ^{EU}	3.71
C-UN-HSC-W-23-8 (1)	8	9	2.60	(b) *	-2.19	2.18	3.99 ^{EU} /2.20 ^{PC}	-3.98 ^{EU} /-2.20 ^{PC}	4.76
C-UN-HSC-W-23-8 (2)	8	9	2.39	(b)	-2.02	2.01	4.17 ^{EU} /2.38 ^{PC}	-4.16 ^{EU} /-2.37 ^{PC}	4.76
C-UN-HSC-W-40-8 (1)	8	29	3.21	(b)+(a) *	-2.71	2.70	6.45 ^{EU} /3.85 ^{PC}	-6.43 ^{EU} /-3.83 ^{PC}	4.75
C-UN-HSC-W-40-8 (2)	8	29	2.61	(b)	-2.20	2.19	6.95 ^{EU} /4.35 ^{PC}	-6.93 ^{EU} /-4.34 ^{PC}	4.75
C-UN-HSC-W-23-16 (1)	16	17	3.39	(b)+(a) *	-2.86	2.85	4.72 ^{EU} /2.55 ^{PC}	-4.70 ^{EU} /-2.54 ^{PC}	4.76
C-UN-HSC-W-23-16 (2)	16	17	2.48	(b)	-2.09	2.08	5.49 ^{EU} /3.32 ^{PC}	-5.47 ^{EU} /-3.30 ^{PC}	4.76
C-UN-HSC-W-40-16 (1)	16	57	3.09	(b)	-2.61	2.60	8.73 ^{EU} /5.56 ^{PC}	-8.70 ^{EU} /-5.54 ^{PC}	4.95
C-UN-HSC-W-40-16 (2)	16	57	3.56	(b)+(a) *	-3.00	2.99	8.33 ^{EU} /5.16 ^{PC}	-8.31 ^{EU} /-5.14 ^{PC}	4.95
C-SL-HSC-W-c-0 (1)	control	1	14.12	(b)+(c)	4.13	-4.11	5.34 ^{EU}	-5.32 ^{EU}	3.71
C-SL-HSC-W-23-16 (1)	16	17	9.64	(b)	2.82	-2.81	5.63 ^{EU}	-5.61 ^{EU}	4.76
C-SL-HSC-W-23-16 (2)	16	17	10.96	(b)+(a) *	3.20	-3.19	6.01 ^{EU}	-5.99 ^{EU}	4.76
C-SL-HSC-W-40-16 (1)	16	50.6	11.74	(b)	3.43	-3.42	7.60 ^{EU}	-7.57 ^{EU}	4.95
C-SL-HSC-W-40-16 (2)	16	50.6	10.52	(b)	3.08	-3.07	7.24 ^{EU}	-7.22 ^{EU}	4.95
C-SL-HSC-W-23-71 (1)	71	72	10.29	(b)+(a)	3.01	-3.00	7.58 ^{EU}	-7.56 ^{EU}	4.88
C-SL-HSC-W-23-71 (2)	71	72	11.48	(b)+(a) *	3.36	-3.35	7.93 ^{EU}	-7.90 ^{EU}	4.88
C-SL-HSC-W-40-71 (1)	71	221	15.21	(b)+(a) *	4.45	-4.43	9.53 ^{EU} /7.84 ^{PC}	-9.50 ^{EU} /-7.81 ^{PC}	4.88
C-SL-HSC-W-40-71 (2)	71	221	11.00	(b)	3.22	-3.21	8.30 ^{EU} /6.60 ^{PC}	-8.27 ^{EU} /-6.58 ^{PC}	4.88
D-HSC-A/W-c-0 (1)	control	2	5.00	(b)	1.72	-1.71	2.85 ^{EU}	-2.84 ^{EU}	4.40
D-HSC-A/W-23-10 (2)	10	12	12.60	(b)+(a) *	4.34	-4.32	6.26 ^{EU}	-6.22 ^{EU}	5.00
D-HSC-A/W-23-10 (3)	10	12	4.90	(b) *	1.69	-1.68	3.60 ^{EU}	-3.58 ^{EU}	5.00
D-HSC-A/W-40-10 (2)	10	33	6.11	(b) *	2.11	-2.09	4.96 ^{EU}	-4.93 ^{EU}	4.98
D-HSC-A/W-40-10 (4)	10	33	5.09	(b)+(d) *	1.75	-1.74	4.61 ^{EU}	-4.58 ^{EU}	4.98
D-HSC-A/W-40-20 (1)	20	64	4.30	(b)	1.48	-1.47	5.12 ^{EU}	-5.09 ^{EU}	4.89
D-HSC-A/W-40-20 (2)	20	64	5.99	(b)+(a) *	2.06	-2.05	5.70 ^{EU}	-5.67 ^{EU}	4.89
D-HSC-A/W-40-35 (3)	35	110.	7.43	(b)+(d)	2.56	-2.55	6.84 ^{EU}	-6.80 ^{EU}	5.05
D-HSC-A/W-40-35 (4)	35	110.	13.20	(b)+(a) *	4.55	-4.52	8.83 ^{EU}	-8.78 ^{EU}	5.05
D-HSC-A/W-23-46 (2)	46	48	5.20	(b) *	1.79	-1.78	5.00 ^{EU}	-4.97 ^{EU}	4.91
D-HSC-A/W-23-46 (4)	46	48	15.24	(b)	5.25	-5.22	8.45 ^{EU}	-8.41 ^{EU}	4.91
D-HSC-A/W-40-46 (1)	46	144.	17.78	(b)+(a) *	6.13	-6.09	10.66 ^{EU}	-10.60 ^{EU}	5.06
D-HSC-A/W-40-46 (2)	46	144.	9.82	(b)+(a)	3.38	-3.36	7.92 ^{EU}	-7.87 ^{EU}	5.06

113

114 **Notes:**

115 1) *a-b-c-d (e)*, where *a* denotes the material group (C-SL, C-UN and D), *b* denotes the concrete mix,
 116 HSC-W or HSC-A/W, *c* denotes the exposure temperature (23 or 40°C) or a control specimen (c), *d* denotes the
 117 exposure time and (*e*) the number of the tested specimen.

118 2) * denotes bond failure inspection with microscope

119 3) ^{EU} denotes uncracked elastic thick walled analysis and ^{PC} denotes partly cracked elastic stage

120 4) experimental bond failure (a) denotes a concrete radial cracking, (b) failure in the sand particles, (c)
 121 failure at the interface between the sand coating layer and the core tendon, (d) failure in the body of the CFRP
 122 tendon and (e) concrete pull out failure.

123

124

125 developed shear stresses due to friction between concrete and steel. However, simulating concrete as a thick-
126 walled cylinder has been proved to be accurate by Bossio et al. [48] when finite Element (FE) results of a
127 cylindrical simplified model and real RC members were compared.

128

129 *3.2 Ultimate bond strength model for FRP in NSC or HSC*

130 The predicted combined effects of concrete shrinkage, CFRP tendon swelling and matrix softening and pull out
131 load appear to be generally consistent with the observed failure modes. Yet the bond strength seems not to be
132 proportionally linearly related to the bond radial component and even greater deviations would be expected if
133 matrix plasticisation and concrete cracking were not taken into account. To understand the effect of matrix
134 degradation, shrinkage, combined swelling and shrinkage effects and sand coating layer variations (in [35]) on
135 long-term bond strength, each influence is initially taken to be independent, of equal importance and additive.
136 Their combined contribution to the experimental bond strength values of both CFRP and GFRP rods as found in
137 the literature is assessed with a regression analysis.

138 *3.2.1 Input parameters*

139 The additional studies considered here are summarised in Table 7. Data regarding the level of sand coverage
140 was only available in [35] where an image processing technique was used to infer a sand coating layer factor.
141 For the shrinkage and swelling effects, bond factors were calculated from the ratio of the radial stresses (thick
142 walled analysis) after the specific exposure/curing time to the reference time (see Table 4). The bond strength
143 factors for the plasticisation effects were derived with respect to the reference dry value, τ_o , from Equation 16
144 based on the moisture concentration gradient in the FRP rods. The sand coating layer factor is a parameter
145 representing the number of sand particles in the external sand coating layer of the CFRP tendons (for group C-
146 SL and D in [35]).

147

148

149

150

151

152

154 **Table 7: Experimental studies of FRP rods in NSC**

	Concrete		FRP			Curing/Exposure conditions
	f_c (MPa)	E_c (GPa)	Specimen dimension (mm)	Type	Rod diameter, D (mm)	
Robert & Benmokrane [49]	55-62 ¹	36 ²	200	CFRP/sand coated	19	Initial curing at saturated humidity for 40 days followed by immersion in tap water at 23°C for 180 days. Exposure in tap water for 60, 120 and 180 days at 23°C
Davalos et al. [21]	57-63 ¹	36 ²	150	CFRP/sand blasted & GFRP/sand coated	9	Initial immersion in a curing tank at 23°C for 27 days and exposure in tap water for 90 days at 23°C and 60°C
Sivanendran [41]	36.9	33	100	CFRP uncoated	4.2	Control specimens (1-C-D) were air cured. Exposed specimens were immersed in still water at 23°C for up to 125 days and after 7 days of air curing. The exposed specimen were either unstressed (1-S-W) or low prestressed around 30% f_{tu} (2-S-W-L)
Emparanza et al. [50]	37.2 ¹	31 ²	200	GFRP/sand coated and helically wrapped (Type A), GFRP/helically wrapped (Type B) and GFRP/ribbed (Type C)	10	Initial curing at ambient conditions for 28 days followed by immersion in seawater at 23°C for up to 120 days

155 **Note:** ¹: values after 28 days, ²: after EC2 [34]

156

157 Table 8 shows the experimental and analytically predicted bond strength values for the studies reported in the

158 current work and elsewhere [49, 21, 50, 41]. The bond strength values vary with exposure time and are derived

159 by multiplying the reference bond strength control values at the initiation of the exposure programme

160 (highlighted in bold font in Table 8) by the relevant bond strength factors. The specific concrete strength and

161 curing regime (wet or air curing), the actual concrete dimensions of the bond test specimens, the reported rod diameter

162 and longitudinal Young's modulus of elasticity in each study were considered in the model. The experimental details

163 of each study are tabulated in Table 7. If not reported, the concrete Young's modulus and tensile strength were

164 derived from Eurocode 2 [34] for the relevant concrete grades. The diffusion coefficients for NSC and HSC were
165 derived from Table 2. The diffusion coefficient of each rod and the transverse Young's modulus were fixed as
166 $D_{22}=1.46\times 10^{-10}$ cm²/sec and $E_T=6.16$ GPa (as for group C-SL in [35]), irrespective of the fiber type (carbon versus
167 glass). Saturated bond strength values of $0.83\tau_o$ are assumed for all tendons with the exception of the C-UN group in
168 [35], where $\tau_{sat}=0.71\tau_o$. These assumptions were based on the experimental torsional shear modulus degradation data
169 in [35] for CFRP tendons exposed in water. They are adopted here because they are indicative of matrix plasticisation
170 phenomena. The C-UN group of tendons exhibited higher moisture uptake and shear modulus degradation primarily
171 due to the presence of voids. The curing time was additionally considered in the exposure regime.

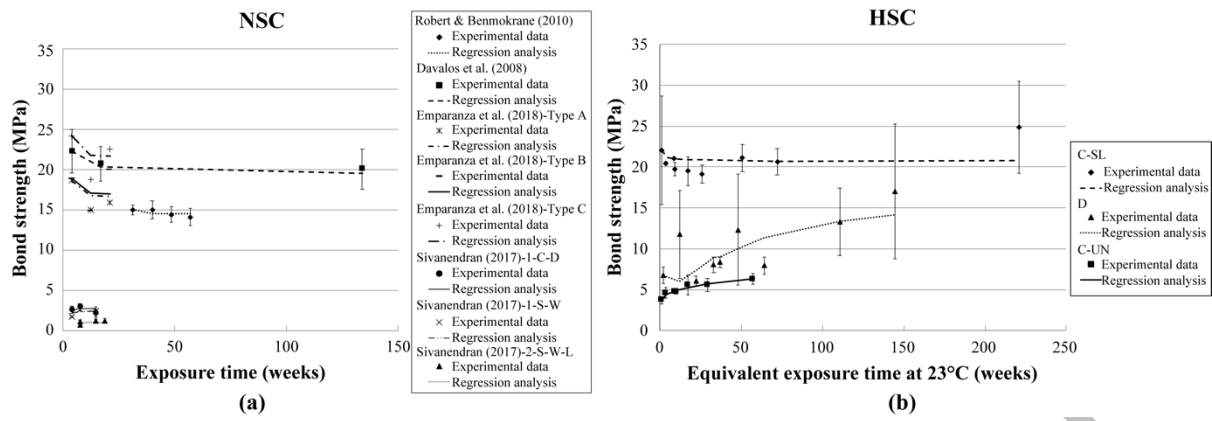
172 3.2.2 Discussion

173

174 The greatest decrease in bond due to matrix plasticisation is predicted for the C-UN group (19%) with respect to
175 its reference value and attributed to the higher diffusivity in this group (higher void content within the core
176 tendon). The bond strength factors due to shrinkage effects potentially reach a plateau at low exposure/curing
177 times when the ultimate concrete shrinkage strain values have been attained. In a few studies (e.g. in [50]) these
178 factors are very low. This is attributed to the curing regime where exposure in water took place after an initial
179 curing period at ambient conditions resulting in a decrease in the shrinkage strain values. The increase in
180 moisture uptake in the FRP rods with exposure time results in an increasing trend of the bond strength factors
181 when the combined effects of swelling and shrinkage are considered. The moisture uptake at saturation has not
182 yet been reached for the exposure times experimentally studied. It can be observed in Table 8 that the combined
183 effect of swelling expansion and concrete shrinkage significantly overestimate the predicted bond strength in all
184 studies irrespective of the concrete grade (NSC or HSC). The competing bond interactions of the considered
185 physical phenomena are analysed in more detail with a regression analysis considering all the listed parameters,
186 τ_{pl} , $\tau_{swell+sh}$, τ_{sh} and τ_{sand} . In Table 9 the parameters that correlate better with the experimental data and satisfy the
187 5% significance F and p level based on the Analysis of Variance (ANOVA) process are summarised for all the
188 studies considered. The plasticisation phenomenon seems to fit best the experimental data for both NSC and
189 HSC within the experimental standard deviation as depicted in Figure 8. This parameter results in the highest R^2
190 values within the 0.05 significance level for the majority of the studies. Direct comparisons between NSC and
191 HSC are difficult since all plasticisation factors are normalised with respect to control values. Indicatively, the
192 D-HSC-A/W group exhibited a 0.98 total reduction factor after 22 weeks of full immersion in water in HSC and
193 a 0.98 factor was calculated for Empananza et al. [50] for a similar exposure time. Differences due to

194 plasticisation phenomena can be distinguished at longer exposure times as shown in the concentration gradients
195 of the C-UN tendons in HSC and NSC (Figure 6c respectively) due to the progressive decrease in the concrete
196 humidity in HSC. Yet, the current analytical data suggests that the matrix softening of the FRP rods due to the
197 exposure in a concrete humid environment can result in a decrease of up to 5% (excluding the C-UN group in
198 [35]). Swelling and shrinkage effects seem to overestimate the long-term bond strength values but are
199 statistically significant in uncoated tendons where a bond increase has been reported and attributed to the bond
200 frictional component. The regression analysis coefficients of the $\tau_{swell+sh}$ parameter in the C-UN group are low
201 compared with τ_{pl} suggesting that the swelling effects are overestimated. The sand coating layer variation is
202 judged to be the leading factor in groups C-SL and D and secondarily shrinkage and matrix degradation effects,
203 as highlighted in [35]. Plasticisation phenomena combined with shrinkage effects were found to influence the
204 results in [41]&[49]. In general, the regression analysis yields a good correlation with only one or two bond
205 strength parameters.

206 The analytical findings presented here rely on data from bond experiments of FRP concrete specimens after
207 exposure in water under unstressed conditions. In structural applications CFRP tendons will be under sustained
208 loading that can lead to accelerated bond degradation. An increase in moisture absorption has been reported in
209 [51] with an increase in the tensile stress level and angle of load application with respect to the fibre direction.
210 This can be attributed to either a higher free volume at the molecular level or matrix cracking. FRP matrix
211 degradation has been observed in [52] due to the combined effects of moisture absorption and sustained loading.
212 Failure of a CFRP prestressed concrete pole under four-point loading and exposed to outdoor conditions for
213 roughly 17 years was reported in [53] and attributed to bond creep. Bond radial cracking and concrete pull out
214 bond failure modes are expected to be negligible in prestressed concrete in the flexural development length. The
215 sustained loading in concrete is expected to affect the concrete moisture diffusion, internal humidity, shrinkage
216 effects and concrete creep and thereby change the shear stresses at the FRP/concrete interface. Moreover,
217 different bond mechanisms act within the transfer length of CFRP prestressed concrete beams and so the degree
218 to which bond durability can affect both the prestressing force and the transfer length should be considered.



219

220

Figure 8: Analytical bond strength degradation predictions for (a) NSC and (b) HSC.

221 **Table 8:** Analytically predicted bond strength values due to plasticisation, swelling and shrinkage effects and level of sand coverage.

Experimental					Analytical predicted										
Specimen	Exposure time (weeks)	Bond strength			Factors				Bond strength						
		τ_{mean} (MPa)	$STDV$ (MPa)	Ratio	Plasticisation	swelling & shrinkage	Shrinkage	sand coating layer	τ_{pl} (MPa)	$\tau_{swell+sh}$ (MPa)	τ_{sh} (MPa)	τ_{sand} (MPa)	$\tau_{regression}$ (MPa)	Ratio	
HSC	Toumpanaki et al. [35] – CFRP-C-SL-HSC-W	1	22.09	6.63	1.00	1.00	1.00	1.00	0.83	22.09	22.09	22.09	22.09	22.09	1.0
		3.5	20.44	0.25	0.93	0.99	1.45	1.59	0.83	21.83	32.07	35.03	22.09	21.21	0.96
		8.7	21.05	0.11	0.95	0.98	2.01	1.57	0.86	21.65	44.33	34.68	22.87	21.03	0.95
		9	19.76	0.83	0.89	0.98	1.91	1.96	0.85	21.65	42.18	43.27	22.62	21.03	0.95
		17	19.53	1.76	0.88	0.98	2.32	2.10	0.85	21.55	51.15	46.30	22.60	20.93	0.95
		25.8	19.17	1.1	0.87	0.97	2.74	1.93	0.82	21.48	60.43	42.61	21.93	20.87	0.94
		50.6	21.1	1.63	0.96	0.97	3.44	2.05	0.86	21.35	75.99	45.17	22.97	20.75	0.94
		72	20.64	1.59	0.93	0.96	3.78	2.26	0.82	21.30	83.40	49.99	21.90	20.70	0.94
		221	24.84	5.64	1.12	0.96	2.80	2.24	0.84	21.35	61.79	49.53	22.49	20.74	0.94
	Toumpanaki et al. [35] – CFRP-D-HSC-A/W	2	6.75	0.98	1.00	1.00	1.00	1.00	0.80	6.75	6.75	6.75	6.75	6.75	1
		12	11.77	5.37	1.74	0.99	1.69	1.60	0.81	6.70	11.43	10.80	6.83	5.99	0.9
		22	6.05	0.63	0.90	0.98	2.08	1.72	0.76	6.64	14.04	11.59	6.41	7.35	1.1
		33	8.07	0.95	1.20	0.98	2.53	1.57	0.79	6.59	17.05	10.60	6.67	8.93	1.3
		37	8.36	0.65	1.24	0.97	2.55	1.77	0.79	6.57	17.22	11.97	6.67	9.01	1.3
		48	12.33	6.81	1.83	0.97	2.83	1.78	0.85	6.53	19.12	12.04	7.17	10.01	1.5
		64	7.94	1.09	1.18	0.96	3.22	1.67	0.83	6.49	21.72	11.24	7.00	11.37	1.7
		110.5	13.29	4.14	1.97	0.95	3.79	1.71	0.81	6.42	25.56	11.52	6.83	13.38	2.0
		144.6	16.99	8.25	2.52	0.95	4.01	1.71	0.80	6.40	27.05	11.57	6.75	14.16	2.1
	1	3.73	0.44	1.00	1.00	1.0	1.0	N/A	3.73	3.73	3.73	N/A	3.73	1.0	

		3.5	4.59	0.64	1.23	0.86	1.1	1.5	N/A	3.21	3.93	5.49	N/A	4.37	1.2
		9	4.73	0.28	1.27	0.84	1.5	1.8	N/A	3.14	5.41	6.76	N/A	4.82	1.3
	Toumpanaki et al. [35] –CFRP - C-UN-HSC-W	9.75	4.79	0.36	1.28	0.84	1.5	1.4	N/A	3.13	5.68	5.40	N/A	4.91	1.3
		17	5.57	1.22	1.49	0.83	1.8	1.9	N/A	3.10	6.65	7.20	N/A	5.21	1.4
		29	5.52	0.81	1.48	0.82	2.2	1.8	N/A	3.07	8.07	6.59	N/A	5.67	1.5
		57	6.31	0.63	1.69	0.81	2.7	1.9	N/A	3.02	10.05	6.59	N/A	6.31	1.7
NSC	Robert & Benmokrane [49]	31.4	15	0.60	1.00	1.00	1.0	1.0	N/A	15	15	15	N/A	15.0	1.0
		40.0	15	1.14	1.00	1.00	1.12	1.01	N/A	15	16.80	15.21	N/A	14.53	0.97
		48.6	14.4	0.96	0.96	0.99	1.23	1.02	N/A	14.9	18.44	15.35	N/A	14.50	0.97
		57.1	14.1	1.11	0.94	0.99	1.33	1.03	N/A	14.9	19.92	15.42	N/A	14.47	0.96
	Davalos et al. [21] - CFRP	4	22.3	2.7	1.00	1.00	1.00	1.0	N/A	22.3	22.3	22.3	N/A	22.3	1.00
		17	20.7	2.1	0.93	0.98	1.79	1.34	N/A	21.9	39.76	29.76	N/A	20.31	0.91
		134	20.0	2.5	0.90	0.95	2.84	1.43	N/A	21.1	63.15	31.83	N/A	19.55	0.88
	Davalos et al. [21] - GFRP	4	23.4	0.6	1.0	1.00	1.00	1.0	N/A	23.4	23.4	23.4	N/A	23.4	1.00
		17	18.8	2.3	0.8	0.98	1.79	1.34	N/A	23.0	41.83	31.31	N/A	21.36	0.91
	Emparanza et al. [50]- GFRP-Type A	4	18.6	N/A	1.0	1.00	1	1	N/A	18.60	18.6	18.6	N/A	18.6	1.0
		12.6	15.0	N/A	0.80	0.99	4.47	0.09	N/A	18.39	83.09	1.64	N/A	16.76	0.90
		21.1	15.9	N/A	0.85	0.98	5.02	0.09	N/A	18.26	93.45	1.75	N/A	16.65	0.89
	Emparanza et al. [50]- GFRP-Type B	4	18.9	N/A	1.00	1.00	1.0	1	N/A	18.9	18.9	18.9	N/A	18.9	1.00
		12.6	14.9	N/A	0.79	0.99	4.47	0.09	N/A	18.69	84.43	1.66	N/A	17.03	0.90
		21.1	20.0	N/A	1.06	0.98	5.02	0.09	N/A	18.56	94.95	1.78	N/A	16.91	0.89
	Emparanza et al. [50]- GFRP-Type C	4	24.2	N/A	1.00	1.00	1.0	1	N/A	24.20	24.2	24.2	N/A	24.20	1.00
		12.6	18.7	N/A	0.77	0.99	4.47	0.09	N/A	23.93	108.10	2.13	N/A	21.81	0.90
		21.1	22.5	N/A	0.93	0.98	5.02	0.09	N/A	23.76	121.58	2.27	N/A	21.66	0.89
	Sivanendran [41] – control- CFRP-unstressed	3	2.6	0.47	1.00	1.00	1	1	N/A	2.6	2.6	2.6	N/A	2.6	1.0
		6.7	2.9	0.48	1.14	0.99	1.6	1.2	N/A	2.5	4.2	3.0	N/A	2.8	1.08
13.9		2.1	0.48	0.83	0.98	3.0	1.3	N/A	2.5	7.6	3.3	N/A	2.7	1.07	

Sivanendran (2017)- CFRP-wet unstressed conditions	3	1.7	0.14	1.00	1.00	1.0	1	N/A	1.7	1.7	1.7	N/A	1.7	1.0
	6.7	2.6	0.20	1.51	0.99	1.3	1.2	N/A	1.7	2.21	2.01	N/A	2.4	1.05
	13.9	2.4	0.57	1.39	0.98	1.7	1.3	N/A	1.7	2.84	2.23	N/A	2.4	1.08
Sivanendran [41] - CFRP - low prestressed conditions	6.7	1.11	0.20	1.00	1.00	1	1	N/A	1.11	1.11	1.11	N/A	1.11	1.00
	6.7	0.7	0.28	0.66	1.00	3.7	0.1	N/A	1.11	4.12	0.07	N/A	1.02	0.7
	13.9	1.2	0.19	1.05	0.99	4.8	0.1	N/A	1.10	5.34	0.08	N/A	1.01	0.69
	13.9	1.2	0.29	1.06	0.98	3.1	0.1	N/A	1.09	3.45	0.08	N/A	1.00	0.69

222
223
224

Table 9: Analytical bond strength durability model –Regression analysis

Experimental studies	Regression analysis coefficients				P-value				Significance <i>F</i>	<i>R</i> ²
	τ_{pl}	$\tau_{swell+sh}$	τ_{sh}	τ_{sand}	τ_{pl}	$\tau_{swell+sh}$	τ_{sh}	τ_{sand}		
C-SL-HSC-W*	0.97	N/A	N/A	N/A	1.4E-07	N/A	N/A	N/A	1.1E-06	0.99
C-SL-HSC-W	N/A	N/A	N/A	0.93	N/A	N/A	N/A	9.9E-08	8.3E-07	0.99
Toumpanaki et al. [35]	D-HSC-A/W*	N/A	0.52	N/A	N/A	1.1E-05	N/A	N/A	4.3E-05	0.97
	D-HSC-A/W	N/A	N/A	0.93	N/A	N/A	6.6E-05	N/A	2.0E-04	0.91
	D-HSC-A/W	N/A	N/A	N/A	1.54	N/A	N/A	N/A	3.0E-04	0.90
C-UN-HSC-W*	0.94	0.35	N/A	N/A	7.0E-03	1.0E-02	N/A	N/A	8.0E-04	1.00
C-UN-HSC-W	N/A	N/A	0.82	N/A	N/A	N/A	1.8E-06	N/A	1.4E-05	0.99
Robert & Benmokrane [49]*	0.97	N/A	N/A	N/A	3.0E-04	N/A	N/A	N/A	1.0E-02	1.00
Robert & Benmokrane [49]	4.07	N/A	-3.02	N/A	3.0E-02	N/A	4.0E-02	N/A	3.7E-09	1.00
Davalos et al. [21]*	0.93	N/A	N/A	N/A	2.0E-04	N/A	N/A	N/A	2.0E-03	0.99
Sivanendran [41]	1.09	N/A	N/A	N/A	1.3E-06	N/A	N/A	N/A	4.0E-06	0.95
Sivanendran [41]*	0.89	N/A	0.42	N/A	5.0E-03	N/A	5.0E-02	N/A	2.0E-03	0.98
Empananza et al. [50]*	0.91	N/A	N/A	N/A	6.0E-08	N/A	N/A	N/A	3.7E-07	0.99

225

Note: * regression analysis coefficients considered in Table 8.

226 **4 Conclusions**

227 The phenomena that lead to bond failures of CFRP tendons in concrete exposed to water are complex as there
228 are many competing mechanisms. The tendon swelling expansion due to the internal concrete relative humidity,
229 temperature effects, concrete autogeneous shrinkage, Poisson's ratio effects and bond bearing stresses need to
230 be considered. A model is proposed for the prediction of the long-term bond failure mechanisms and bond
231 strength of sand coated or uncoated FRP reinforcement in concrete. The model considers an elastic uncracked
232 and partly cracked thick walled analysis. Matrix plasticisation phenomena are incorporated by adapting a
233 torsional shear modulus degradation approach.

234 The model predictions of the bond failure modes correlated fairly well with experimental results on CFRP
235 tendons in high strength concrete as presented in [35] where cases of radial cracking were confirmed using
236 visual microscopic analyses. Time-dependent phenomena such as the concrete autogeneous shrinkage and any
237 transverse swelling of a CFRP tendon expansion due to embedment in a moist concrete environment seems to
238 influence whether concrete radial cracks are associated with pull-out failures. The model was also used to
239 predict the long-term bond strength by taking into account matrix swelling effects, time dependent concrete
240 shrinkage, plasticisation and sand coating layer variations in CFRP tendons. The first two parameters are
241 assumed to affect the bond frictional component, as derived from the thick walled analysis, and the last two
242 parameters are related to mechanical interlocking bond effects. Matrix plasticisation seems to show the strongest
243 correlation with experimental bond durability data as found in the literature for both normal and high strength
244 concrete. The combination of plasticisation and swelling and shrinkage effects appear to be more significant for
245 the bond strength values of uncoated tendons and this was believed to be due to the influence of these effects on
246 the bond frictional component. Deviations from the analytical predictions are attributed to a possible
247 overestimation of the moisture uptake and swelling expansion in the CFRP tendons, differences in concrete
248 strength, and sand coating layer variability. The introduction of environmental bond factors in the design of FRP
249 reinforced and prestressed concrete structures is needed to account for matrix plasticisation in the FRP rods and
250 long-term effects between the two materials.

251 **5 Acknowledgements**

252 We are grateful to SACAC Ltd for their technical and financial assistance. The financial support from the
253 Onassis Foundation (ET) is also greatly appreciated.

254 **6 Data availability statement**

255 Additional raw/processed data required to reproduce these findings can be found in Toumpanaki, E., Lees,
256 J.M.L. and Terrasi, G.P. (2020). ‘Moisture concentration gradients in concrete and FRP tendons’, Mendeley
257 Data, V1, doi: 10.17632/7rs5mxmpz6.1.

258 **7 References**

- 259 [1] Koch, G.H., Brongers, M.P.H., Neil, G.T., Virmani, Y.P., and Payer, J.H. (2002). “Corrosion costs and
260 preventive strategies in the United States.” *Report FHWA-RD-01-156*, NACE.
- 261 [2] Abdelrahman, A.A., Tadros, G., and Rizkalla, S.H. (1995). “Test model for the first Canadian smart
262 highway bridge.” *ACI Struct. J.*, 92(4), 451-458.
- 263 [3] Terrasi, G.P. and Lees, J.M. (2003). “CFRP prestressed concrete lightning columns”, ACI SP-215, 55-74
- 264 [4] ACI 440.1R-15 (2015). “Guide for the Design and Construction of Structural Concrete Reinforced with Fiber-
265 Reinforced Polymer (FRP) Bars” American Concrete Institute, Farmington Hills, MI, USA.
- 266 [5] CSA S806-12:R2017 (2017). Design and construction of building structures with fibre-reinforced polymers.
267 Canadian Standards Associations (CSA Group).
- 268 [6] JSCE (1997). “Recommendation for Design and Construction of Concrete Structures using Continuous Fiber
269 Reinforcing Materials.” Concrete Engineering Series 23, Japan Society of Civil Engineers, Tokyo, Japan
- 270 [7] CEB-FIP (2007). “fib Bulletin No. 40, FRP reinforcement in RC structures.” Comité Euro-International du
271 Beton, Lausanne, Switzerland, 160 pp.
- 272 [8] CEB-FIP (2012). “fib Bulletin No. 65, Model Code for Concrete Structures 2010-Final draft, Volume 1”
273 Comité Euro-International du Beton, Lausanne, Switzerland, 350 pp.
- 274 [9] Burgoyne, C. and Balafas, I. (2007). “Why is FRP not a financial success?” *Proc., 8th Int. Symp. on FRPs for*
275 *Reinforced Concrete Structures (FRPRCS-8)*, T. Triantafillou ed., University of Patras, Greece, 1-10.
- 276 [10] Toumpanaki, E., Lees, J.M. and Terrasi, G.P. (2015). “Shear Modulus of Cylindrical CFRP Tendons
277 Exposed to Moisture”, *J. Compos. for Constr.*, 19(3), 12p.
- 278 [11] Scott, P., and Lees, J.M. (2012). “Effect of solution exposure on the combined axial-shear behaviour of
279 unidirectional CFRP rods.” *Composites Part A*, 43(9), 1599-1611.
- 280 [12] Abanilla, M.A, Karbhari, V.M., and Li, Y. (2006). “Interlaminar and intralaminar durability characterization of
281 wet layup carbon/epoxy used in external strengthening.” *Composites: Part B*, 37(7-8), 650-661.
- 282 [13] Aiello, M.A., Focacci, F., and Nanni, A. (2001). “Effects of thermal loads on concrete cover of fiber-
283 reinforced polymer reinforced elements: theoretical and experimental analysis.” *ACI Mater. J.*, 98(4), 332–339.

- 284 [14] Sen, R., Shahawy, M., Sukumar, S., and Rosas, J. (1999). "Durability of carbon fiber reinforced polymer
285 (CFRP) pretensioned elements under tidal/thermal cycles." *ACI Struct. J.*, 96(3), 450-457.
- 286 [15] Eurocode 1 (EC1) (2003). "Actions on structures-Part 1-5: General actions – Thermal actions." *EN 1991-1-5:2003*,
287 Brussels, Belgium.
- 288 [16] Terrasi, G. P., Broenimann, R., and Baettig, G. (2011). "CFRP tendon pre-stress monitoring by resistance
289 measurement in a high performance concrete powerline pylon." *Proc., SMAR 2011, the 1st Middle East Conf.
290 on Smart Monitoring, Assessment and Rehabilitation of Civil Structures*, EMPA, Dübendorf, Switzerland.
- 291 [17] Tompkins, S. S. (1987). "Thermal expansion of selected graphite reinforced polyimide, epoxy- and glass-
292 matrix composites." *Int. J. of Thermophys.*, 1987, 8(1), 119–132.
- 293 [18] Gentry, T.R. (1996). "Thermal compatibility of plastic composite reinforcement
294 and concrete." *Proc. Advanced composite materials in bridges and structures*, M.M. El-Badry ed., Montreal,
295 Canadian Society for Civil Engineering, 149–156.
- 296 [19] Maluk, C., Terrasi, G.P., Bisby, L. Stutz, A. and Hugi, E. (2015). "Fire Resistance Tests on Thin CFRP
297 Prestressed Concrete Slabs" *Constr. Build. Mater.*, 101(1), 558-571.
- 298 [20] Scott, P., and Lees, J.M. (2009). "Uptake-induced swelling and thermal expansion of CFRP tendons." *Structures
299 and Buildings*, 162(4), 263-273.
- 300 [21] Davalos, J.F, Chen, Y., and Ray, I. (2008). "Effect of FRP bar degradation on interface bond with high strength
301 concrete." *Cem. Concr. Compos.*, 30(8), 722-730.
- 302 [22] Larrard, F., Schaller, I., and Fuchs, J. (1993). "Effect of bar diameter on the bond strength of passive
303 reinforcement in high-performance concrete." *ACI Mater. J.*, 90(4), 333–339.
- 304 [23] Sayed, A.F., Foret, G., and Le Roy, R. (2011). "Bond between carbon fibre-reinforced polymer (CFRP)
305 bars and ultra high performance fibre reinforced concrete (UHPFRC): Experimental study." *Constr. Build.
306 Mater.*, 25(2), 479–485.
- 307 [24] Yoo, D.Y., Park, J.J., Kim, S.W., and Yoon, Y.S. (2014). "Influence of reinforcing bar type on autogenous
308 shrinkage stress and bond behavior of ultra high performance fiber reinforced concrete." *Cem. Concr. Compos.*,
309 48, 150–161.
- 310 [25] Achillides, Z., and Pilakoutas, K. (2004). "Bond behavior of fiber reinforced polymer bars under direct
311 pullout conditions." *J. Compos. for Constr.*, 8(2), 173–181.

312 [26] Tepfers, R. (1997). "Bond of FRP reinforcement in concrete. A state-of- the-art report in preparation."
313 Chalmers University of Technology, Work No.15, American Concrete Institute (ACI), Bond and Development
314 for Reinforcement, SP-180, 493-508.

315 [27] Timoshenko, S., and Goodier, J.N. (1970). *Theory of Elasticity*, 3rd Ed., McGraw-Hill, New York.

316 [28] Tepfers (1989). 'Cracking of concrete cover along anchored deformed reinforcing bars.' Magazine of
317 Concrete Research, 31(106), 3-12.

318 [29] Powers, T.C. (1949). 'The non-evaporable water content of hardened Portland cement paste: its significance
319 for concrete research and its method of determination.' *ASTM Bul. No 158*, 68-76.

320 [30] Zhang, J., Gao, Y. and Han, Y. (2012). "Interior Humidity of Concrete under Dry-Wet Cycles". *J. Mater.*
321 *Civ. Eng.*, 24(3), 289-298.

322 [31] Crank, J. (1979). *The Mathematics of Diffusion*. 2nd Edition, Oxford University Press, Oxford, UK.

323 [32] ASTM (2013). "Standard test method for measurement of rate of absorption of water by hydraulic-cement
324 concretes." ASTM C1585-13, West Conshohocken, PA.

325 [33] Toumpanaki, E. (2015). "Durability and bond performance of CFRP tendons in high strength concrete."
326 PhD Thesis, University of Cambridge

327 [34] Eurocode 2 (EC2) (2004). "Design of concrete structures-Part 1-1: General rules and rules for buildings." *ENV*
328 *1992-1-1:2004*, Brussels, Belgium.

329 [35] Toumpanaki, E., Lees, J.M. and Terrasi, G.P. (2018). "Bond Durability of Carbon Fiber-Reinforced
330 Polymer Tendons Embedded in High-Strength Concrete.", *J. Compos. for Constr.*, 22(5), 17 p.

331 [36] Scott, P. (2009). "Aspects of CFRP Prestressed Concrete Durability in the Marine Environment." PhD
332 thesis, University of Cambridge, UK.

333 [37] Terrasi, G.P., Affolter, C. and Barbezat, M. (2011). "Numerical optimisation of a compact and reusable
334 pretensioning anchorage system of CFRP tendons.", 15(2), 126-135.

335 [38] Neville, A.M. (2011). *Properties of concrete*. 5th Edition. Pearson Education Limited.

336 [39] Castro, J., Bentz, D., and Weiss, J. (2011). "Effect of sample conditioning on the water absorption of
337 concrete." *Cem. Concr. Compos.*, 33(8), 805–813.

338 [40] Terrasi, G.P., Bisby, L., Barbezat, M., Affolter, C., and Hugi, E. (2012). "Fire behavior of thin CFRP
339 pretensioned high-strength concrete slabs." *J. Compos. for Constr.*, 16(4), 381–394.

340 [41] Sivanendran, S. (2017). "CFRP Prestressed Concrete Exposed to Moisture." PhD thesis, University of
341 Cambridge, UK.

342 [42] Augi, J.M. and Berger, A.E. (1976). "The Effect of Moisture on Carbon Fiber Reinforced Epoxy Composites |
343 Diffusion." Technical Report. Naval Surface Weapons Centre.

344 [43] Adamson, M. J. (1980). "Thermal Expansion and Swelling of Cured Epoxy Resin used in Graphite/Epoxy
345 Composite Materials." *J. Mater. Sci.*, 15(7), pp. 1736-1745. DOI:10.1007/BF00550593.

346 [44] Vanlandingham, M. R., Eduljee, R. F., and Gillespie, J. W. (1999). "Moisture Diffusion in Epoxy
347 Systems." *J. Appl. Polym. Sci.*, 71(5), 787-798.

348 [45] Cairns, D. and Adams, D. (1983). "Moisture and Thermal Expansion Properties of Unidirectional Composite
349 Materials and the Epoxy Matrix" *Journal of Reinforced Plastics and Composites*, 2(4), 239-255

350 [46] Helbling, C.S. and Karbhari, V.M. (2008). "Investigation of the Sorption and Tensile Response of
351 Pultruded E-Glass/Vinylester Composites Subjected to Hygrothermal Exposure and Sustained Strain." *J. Reinf.*
352 *Plast. Compos.*, 27(6), 613-626.

353 [47] Chermi, L. and Val, D.V. (2011). "Prediction of corrosion-induced cover cracking in reinforced concrete
354 structures." *Constr. Build. Mater.*, 25, 1854-1869.

355 [48] Bossio, A., Monetta, T., Bellucci, F., Lignola, G.P. and Prota, A. (2015). "Modelling of concrete cracking due to
356 corrosion process of reinforcement bars". *Cem. Concr. Res.*, 71, 78-92.

357 [49] Robert, M. and Benmokrane, B. (2010). 'Effect of aging on bond of GFRP bars' *Cem. Concr. Compos.*,
358 32(6), 461-467.

359 [50] Emparanza, A.R., Basalo, F., Kampmann, R. and Nanni, A. (2018). 'Bond Evaluation of GFRP reinforcing bars
360 embedded in concrete under aggressive environments', *Proc. CICE 2018:9th International Conference on Fibre-*
361 *Reinforced Polymer (FRP) Composites in Civil Engineering*, Paris, France, 17-19 July.

362 [51] Neumann, S. and Marom G. (1987). 'Prediction of Moisture Diffusion Parameters in Composite Materials Under
363 Stress', *J. Compos. Mater.*, 21(1), 68-80.

364 [52] Karbhari, V.M., Stachowski, C. and Wu, L. (2007). 'Durability of Pultruded E-Glass/Vinylester under
365 Combined Hygrothermal Exposure and Sustained Bending', *J. Mater. Civil Eng.*, 19(8), 665-673.

366 [53] Terrasi, G.P., Meier, U. and Affolter, C. (2014). 'Long-Term Bending Creep Behavior of Thin-Walled CFRP
367 Tendon Pretensioned Spun Concrete Poles', *Polymers*, 6(7), 2065-2081.

368 [54] Tepfers, R. (1973). A Theory of Bond Applied to Overlapped Tensile Reinforcement Splices for Deformed Bars,
369 PhD Thesis. Work No 723, Publication No: 73:2. Division of Concrete Structures, Chalmers University of
370 Technology, Göteborg, Sweden

371